J. Mech. Phys. Solids 194 (2025) 105901

Contents lists available at ScienceDirect

Journal of the Mechanics and Physics of Solids

journal homepage: www.elsevier.com/locate/jmps

Analysis of mode I crack propagation in glassy polymers under cyclic loading using a molecular dynamics informed continuum model for crazing

Tobias Laschuetza *, Thomas Seelig

Institute of Mechanics, Karlsruhe Institute of Technology, Kaiserstrasse 12, 76131 Karlsruhe, Germany

ARTICLE INFO

Keywords:
Craze
Cyclic loading
Micromechanical continuum model
Fracture
Polymeric material
Crack tip plasticity

ABSTRACT

Craze and crack propagation in glassy polymers under cyclic mode I loading are investigated by employing a recently developed continuum-micromechanical model for crazing. This model accounts for the local morphology change from microvoids to fibrils during craze initiation, viscoplastic drawing of bulk material into fibrils, and viscoelastic creep recovery of the fibrillated craze matter during unloading. To ensure consistency between the bulk and craze model parameters, the material parameters of the craze model are normalised and calibrated based on a hybrid approach integrating experimental findings from the literature and molecular dynamics results. This yields a generic, yet representative glassy polymer response.

In the framework of 2D plane strain finite element simulations, we study brittle as well as ductile glassy polymers and assess the results by drawing comparisons to the experimental and numerical literature. For brittle materials, characterised by a purely elastic bulk behaviour, the model reproduces craze characteristics such as the craze opening contour, the craze length-to-width ratio, a double stress peak at the craze and crack tip, and a non-proportional stress redistribution during loading-unloading cycles. In ductile glassy polymers, the interaction of shear yielding in the bulk and crazing along the ligament is analysed. In particular, shear bands emanate from the crack tip in each loading cycle and arch forward towards the craze. This plastic zone shares resemblance to the so-called *epsilon-shaped deformation zone*. The current simulations capture *normal fatigue crack propagation*, where craze and crack growth occur near the peak load in every cycle and the craze length remains relatively constant across the loading cycles. Moreover, findings from this study suggest that plasticity-induced unloading of the craze adjacent to the crack tip impedes crack growth.

1. Introduction

Crack growth in glassy polymers is typically accompanied by crazing in a narrow zone ahead of the crack tip. This damage process involves the formation and coalescence of microvoids, fibrillation of the polymer material in between and drawing of new material into the load-bearing fibrils. By ultimate rupture of the latter the craze zone locally turns into a crack. The energy dissipated in this *process zone* determines the fracture toughness of the material and hence is of practical importance. Crazing may occur as the sole inelastic deformation process in brittle glassy polymers such as polystyrene (PS), or it may take place in conjunction with shear yielding of the surrounding material in more ductile polymers such as polycarbonate (PC). Crazing in the course of crack

* Corresponding author.
E-mail address: tobias.laschuetza@kit.edu (T. Laschuetza).

https://doi.org/10.1016/j.jmps.2024.105901
Received 18 July 2024; Received in revised form 17 September 2024; Accepted 6 October 2024

Available online 18 October 2024

propagation under monotonic as well as cyclic (e.g. fatigue) loading conditions has been subject of numerous experimental studies; see, e.g., the review articles in Kambour (1973), Kausch (1983, 1990), Narisawa and Yee (1993), Haward and Young (1997). Some key findings in case of cyclic loading are as follows: The fibrillated craze matter displays a pronounced viscoelastic behaviour in terms of deformation and creep recovery during the loading and unloading stages (Kambour and Kopp, 1969; Hoare and Hull, 1972). Compressive stresses at a crack tip upon unloading, which are likely to result from folding (or jamming) of the loose-hanging craze fibrils, are reported e.g. in Schirrer et al. (1984), Pruitt and Suresh (1993). Moreover, in the range of low loading amplitudes crack advance may take place not in every cycle but by jumps after remaining stationary for hundreds of fatigue cycles, which is referred to as *discontinuous* or *retarded* fatigue crack growth, e.g. Skibo et al. (1977), Könczöl et al. (1990), in contrast crack advance in each cycle is understood as *normal* fatigue crack growth. During retarded fatigue crack growth and between successive crack jumps, the thickening of the craze in the first half of its lifetime is primarily due to fibril drawing, whereas in the second half it is predominantly influenced by fibril creep, as reported in Könczöl et al. (1990). Crack growth in ductile glassy polymers under cyclic loading may exhibit an interesting interaction of crazing and shear yielding which gives rise to the occurrence of a regularly spaced ε-shaped plastic zone accompanying the advancing crack tip (Mills and Walker, 1980; Takemori, 1982). Such an interaction is understood to significantly increase the material's load bearing capacity under cyclic (fatigue) loading conditions (Takemori, 1990).

Theoretical-computational studies of craze and crack propagation in glassy polymers have followed various modelling approaches with the majority restricted to monotonic loading conditions. Early studies employed a Barenblatt–Dugdale type representation of the craze zone ahead of an advancing crack tip, e.g. Cotterell (1968), Kramer and Hart (1984), Imai and Ward (1985). Other approaches, e.g. Wang and Kramer (1982), Bevan et al. (1986), Ungsuwarungsri and Knauss (1988), Pulos and Knauss (1998), aimed at determining the mechanical response of the craze matter by computing the normal stress distribution along a craze in a linear elastic medium from the measured opening displacement profile (craze contour). It has, however, been shown in Warren et al. (1989) that in this approach small deviations in the input displacement profile give rise to significant changes in the computed stress. Fatigue crack propagation in polymers was investigated, e.g., in Maiti and Geubelle (2005) who utilised a phenomenological cohesive zone model and focused on the overall response of the fracture process in terms of Paris' law. A more advanced cohesive zone model that incorporates physical details of the crazing process such as initiation and drawing of material into fibrils until ultimate breakdown has been developed by Van der Giessen and co-workers (Tijssens et al., 2000b). Utilising this model, mode I craze and crack propagation under monotonic loading was studied in brittle (elastic) glassy polymers by Tijssens et al. (2000a) and in ductile glassy polymers by Estevez et al. (2000) who particularly analysed the interaction of shear yielding and crazing. The present work is aimed as a continuation of these studies by focusing on cyclic loading conditions.

Modelling the mechanical response of the fibrillated craze matter under cyclic loading is more involved than under monotonic loading where it is essentially governed by a (rate-dependent) drawing stress. For instance, the structural response of the fibrillated craze matter during unloading and reloading is ambiguous and hence is its proper representation. This includes relaxation and creep recovery during unloading stages when fibril drawing is interrupted, the occurrence of compressive stresses due to fibril jamming as well as cyclic damage accumulation. In order to capture these aspects, a novel continuum-micromechanical model for crazing has recently been developed in Laschuetza and Seelig (2024). In a finite strain setting, the model builds upon micromechanical considerations by Boyce and co-workers (Socrate et al., 2001; Sharma et al., 2008) to distinguish between the already fibrillated and the not yet fibrillated bulk portions of a *representative craze element* and their conversion in the course of the crazing process. In the present work, this model serves as a *traction separation law* in the process zone ahead of a mode I crack initiating and advancing in a glassy polymer under cyclic loading. However, while the model developed in Laschuetza and Seelig (2024) aims to capture important physics of the cyclic crazing process through its micromechanical basis, it still suffers from inconclusive knowledge about the structural response of the craze matter and insufficient calibration methodologies to estimate an adequate material parameter scope. This is an issue as insight into both aspects is difficult to obtain from experiments. However, molecular dynamics simulations might provide remedy. This type of *bottom-up* computational investigation has in the last decades significantly contributed to the understanding of the crazing process and its dependence on macro-molecular characteristics such as the entanglement density; see, e.g. Rottler and Robbins (2003), Venkatesan and Basu (2015), Ge et al. (2017). While these and other studies so far have focused on monotonic loading conditions, molecular dynamics simulations of the crazing process under cyclic loading have only recently been conducted in Laschuetza et al. (2024). Insights from that study verify the structural assumption of string-like craze fibrils in Laschuetza and Seelig (2024). In this work, we utilise and extend results from Laschuetza et al. (2024) to enrich the original crazing model from Laschuetza and Seelig (2024) by adding additional features, e.g. fibril jamming, and by using molecular dynamics simulations to calibrate material parameters, which are not accessible from experiments. The model is then used to study craze and crack growth under cyclic mode I loading, while comparisons to the aforementioned experiments are drawn.

The present work is organised as follows: In Section 2 the micromechanical crazing model is presented and the methodology of the parameter calibration is discussed as well as some numerical aspects. Details on the molecular dynamics based calibration are provided in Appendix A. Finite element simulations of craze and crack growth in glassy polymers under cyclic mode I loading are subject of Sections 3 and 4. Section 3, which also includes the set-up of the boundary value problem and details on the computational treatment, focuses on brittle glassy polymers where the bulk material surrounding the craze and crack is considered linear elastic. The interaction of crazing and shear yielding during crack growth under cyclic loading in ductile glassy polymers is studied in Section 4. The constitutive model utilised to describe finite strain viscoplastic shear yielding in the bulk material is based on the well-known model by Boyce and co-workers (Boyce et al., 1988) in a setting which is briefly presented in Appendix B.

The notation throughout this paper makes use of the standard symbolic bold face representation of vectors and second order tensors as well as the Cartesian index notation of their components.

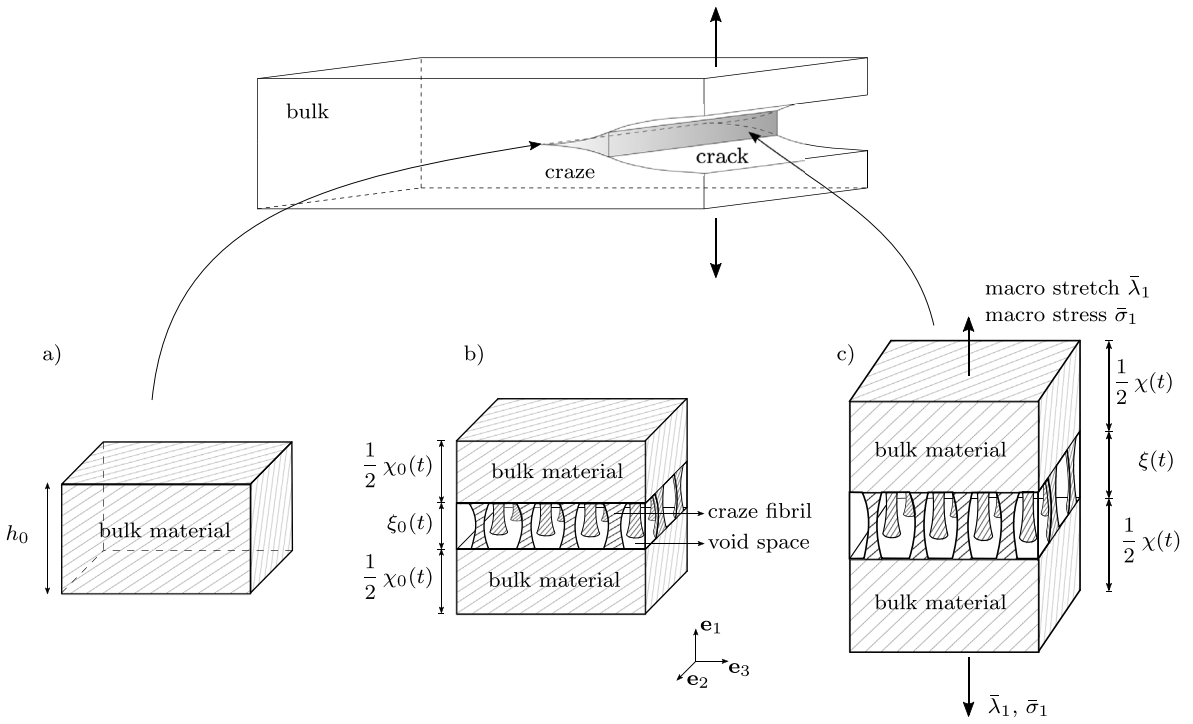

Fig. 1. Schematic of mode I craze and crack growth with different stages of crazing process; (a) prior to craze initiation, (b) unloaded state after craze initiation and (c) loaded state after craze initiation.

2. Continuum-micromechanical model for crazing

The main topic of this paper is the computational investigation of craze and crack growth in glassy polymers under cyclic mode I loading (cf. Fig. 1 top). Therefore, a continuum-micromechanical model for the cyclic craze response developed in Laschuetza and Seelig (2024) is utilised in the present study to provide a macro-scale traction-separation law. This model considers a *representative craze element* where an elementary volume of initial bulk material (Fig. 1(a)) transitions into crazed material with a current unloaded and loaded configuration sketched in Fig. 1(b) and (c), respectively. Details of the model are briefly summarised in the following three subsections, while details on the parameter calibration, the model response and the numerical treatment are provided in Sections 2.4, 2.5 and 2.6, respectively.

2.1. Micromechanical model

Prior to craze initiation, the craze element consists of bulk material of the initial primordial thickness h_0. At some time t after craze initiation, the craze element comprises layers of fibrillated matter with the current unloaded length $\xi_0(t)$ and bulk material with the current unloaded length $\chi_0(t)$ as indicated in Fig. 1(b); the corresponding lengths in the currently loaded configuration are denoted by $\xi(t)$ and $\chi(t)$, respectively (cf. Fig. 1(c)). The complex craze microstructure is idealised by neglecting cross-tie fibrils and considers only string-like fibrils in the direction $\boldsymbol{e}_1$ of the maximum principal stress (Fig. 1). Mass conservation links the thicknesses of the two phases as

$$h_0 = \chi_0 + \frac{\xi_0}{\lambda_c}\,, \tag{1}$$

where λ_c denotes the fibril extension ratio, defined here as the ratio of the constant bulk density ρ_b to the density ρ_c of the fibrillated craze matter:

$$\lambda_c = \frac{\rho_b}{\rho_c}\,. \tag{2}$$

In order to capture the change of ρ_c (and hence λ_c) due to the morphological transition during craze formation from isolated voids to an interconnected void space with isolated fibrils, the extension ratio λ_c is taken to evolve with the unloaded fibril length ξ_0 from $\lambda_c = 1$ (bulk value) to a saturation value $\lambda_c = \lambda_c^*$ that corresponds to mature fibrils. The transition of $\lambda_c(\xi_0)$ is depicted in Fig. 2 where $\xi_{0,\max} = \lambda_c^*\, h_0$ is the unloaded fibril length at rupture and α defines its fraction upon which mature fibrils exist.

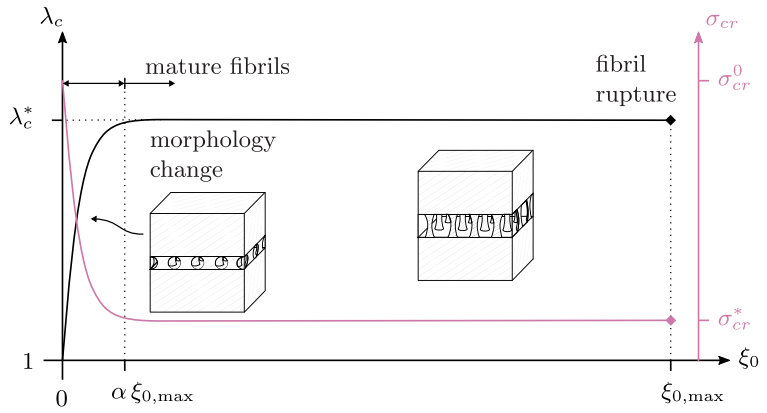

Fig. 2. Phenomenological ansatz to account for effect of morphology change on evolution of extension ratio λ_c as well as drawing resistance σ_{cr} with fibril length ξ_0. Both relations are modelled by similar exponential relations that approximately connect the limit states. Sketches serve to facilitate interpretation of morphology stages.

The stress state in the fibrils is taken as homogeneous and uniaxial, yielding

$$\boldsymbol{\sigma}^f = \sigma^f \boldsymbol{e}_1 \otimes \boldsymbol{e}_1 \,, \tag{3}$$

where σ^f is the Cauchy fibril stress. Likewise, the stress state in the bulk portion of the craze element

$$\boldsymbol{\sigma}^b = \sum_{i=1}^{3} \sigma_i^b \boldsymbol{e}_i \otimes \boldsymbol{e}_i \,, \tag{4}$$

is assumed to be homogeneous. Homogenisation of the layered bulk-craze structure of the element yields through the *rule of mixtures* the macroscopic Cauchy stress $\bar{\boldsymbol{\sigma}}$ as

$$\bar{\boldsymbol{\sigma}} = \sigma_1^b \boldsymbol{e}_1 \otimes \boldsymbol{e}_1 + \frac{\chi}{\chi + \xi} \sum_{i=2}^{3} \sigma_i^b \boldsymbol{e}_i \otimes \boldsymbol{e}_i \,. \tag{5}$$

The overall deformation of the craze element is described by the macroscopic stretch tensor

$$\bar{\boldsymbol{\lambda}} = \sum_{i=1}^{3} \bar{\lambda}_i \boldsymbol{e}_i \otimes \boldsymbol{e}_i \,, \tag{6}$$

which is related to the bulk stretch tensor

$$\boldsymbol{\lambda}^b = \sum_{i=1}^{3} \lambda_i^b \boldsymbol{e}_i \otimes \boldsymbol{e}_i \tag{7}$$

and the fibril stretch in $\boldsymbol{e}_1$-direction $\lambda^f = \xi/\xi_0$ by

$$\bar{\lambda}_1 = \frac{\xi + \chi}{h_0} = \lambda_1^b \frac{\chi_0}{h_0} + \lambda^f \frac{\xi_0}{h_0} \,, \qquad \bar{\lambda}_2 = \lambda_2^b \,, \qquad \bar{\lambda}_3 = \lambda_3^b \,. \tag{8}$$

Force equilibrium in $\boldsymbol{e}_1$-direction and the assumption of isochoric fibril deformation yields (for details see eqs. (10)-(14) in Laschuetza and Seelig (2024))

$$\sigma_1^b = \frac{\sigma^f}{\lambda^f \, \lambda_c \, \lambda_2^b \, \lambda_3^b} \,, \tag{9}$$

which by virtue of (5) provides a coupling between the fibril stress and the macroscopic stress in $\boldsymbol{e}_1$-direction.

The fibril's string-like microstructure suggests that its load-bearing capacity is essentially limited to tension:

$$\sigma^f \geq 0 \,. \tag{10}$$

The notion of string-like fibrils which are *loose* hanging when traction free was corroborated by recent molecular dynamics simulations (Laschuetza et al., 2024), which are also discussed in Appendix A. Additionally, the study revealed a macroscopic compressive stress due to fibril jamming prior to reaching macroscopic compressive deformation, i.e. $\bar{\sigma}_1 < 0$ while $\bar{\lambda}_1 > 1$, which has also been computed from experimentally measured craze profiles (cf., e.g., Bevan et al., 1986). This is incorporated in the present craze model via the ratio

$$\hat{\lambda}_1 = \frac{\xi_0 + \chi_0}{h_0} \,, \tag{11}$$

from which the logarithmic Hencky strain

$$\hat{\varepsilon}_1 = \ln \hat{\lambda}_1 \tag{12}$$

can be computed, which is utilised below in (17). Fibril jamming is then considered for

$$\bar{\varepsilon}_1 = \ln \bar{\lambda}_1 < \beta_c \, \hat{\varepsilon}_1 \tag{13}$$

where β_c is a material parameter that controls the onset of fibril jamming. The craze element's compressive response is modelled by the bulk material.

2.2. Craze initiation, fibril drawing and breakdown

Although various more involved craze initiation criteria exist in the literature, e.g. accounting for the effect of hydrostatic stress, craze initiation in the present work is simply associated with a critical normal stress

$$\sigma_1^b = \sigma_{cr}^0 \, . \tag{14}$$

Upon craze initiation, fibril drawing is described by the flow rule

$$\dot{\xi}_0 = \frac{h_0}{\eta_d} \left\langle \sigma_1^b - \sigma_{cr} \right\rangle \quad \geq 0 \, , \tag{15}$$

which makes use of the standard notation for viscoplastic models with the Macaulay bracket $\langle \cdots \rangle$ and where η_d is the drawing viscosity. The drawing resistance σ_{cr} is taken to decline from an initial value σ_{cr}^0 to a saturation value σ_{cr}^* in order to model the change in stress state in the course of the morphology change between craze initiation by cavitation and fibril drawing (see Fig. 2). This has a similar effect as a craze initiation criterion involving hydrostatic stress as employed, e.g., in Tijssens et al. (2000a), Estevez et al. (2000), Estevez and van der Giessen (2005). The corresponding relation is depicted by the magenta line in Fig. 2.

Fibril breakdown is taken here to occur upon complete consumption of the primordial thickness h_0, i.e. at $\chi_0 = 0$, which yields

$$\xi_{0,max} = \lambda_c^* \, h_0 \, . \tag{16}$$

2.3. Constitutive equations of bulk and craze layer

The material behaviour in the bulk portion of the craze element is given by

$$\boldsymbol{\sigma}^b = 2\mu_b \left(\ln \boldsymbol{\lambda}^b + \frac{\nu_b}{1-2\nu_b} \operatorname{tr} \left[\ln \boldsymbol{\lambda}^b \right] \mathbf{1} \right) , \tag{17}$$

where μ_b and ν_b denote the bulk shear modulus and Poisson's ratio, respectively, and by virtue of (13) $\ln \lambda_1^b = \bar{\varepsilon}_1 - \beta_c \, \hat{\varepsilon}_1$ to account for fibril jamming.

The craze fibrils are modelled as viscoelastic in a three-dimensional finite strain setting. The fibril deformation is for simplicity considered to be isochoric, yielding the fibril stretch tensor $\boldsymbol{\lambda}^f$ as

$$\boldsymbol{\lambda}^f = \lambda^f \boldsymbol{e}_1 \otimes \boldsymbol{e}_1 + \sum_{i=2}^{3} \frac{1}{\sqrt{\lambda^f}} \boldsymbol{e}_i \otimes \boldsymbol{e}_i \, . \tag{18}$$

In accordance with the viscoelastic model shown in Fig. 3, the fibril stretch is multiplicatively decomposed

$$\lambda^f = \lambda^e \, \lambda^v \tag{19}$$

into an elastic λ^e and viscous contribution λ^v, while the fibril stress is additively given by

$$\sigma^f = \sigma_{\mathrm{EC}}^f + \sigma_{\mathrm{NH}}^f \, . \tag{20}$$

The network stress σ_{EC}^f is modelled via the incompressible eight-chain model by Arruda and Boyce (1993)

$$\sigma_{\mathrm{EC}}^f = \frac{\mu_{f,\mathrm{EC}}}{\lambda_C} \frac{\mathcal{L}^{-1}(\lambda_C/\lambda_L)}{\mathcal{L}^{-1}(1/\lambda_L)} \left(\lambda^{f\,2} - \frac{1}{\lambda^f} \right) , \tag{21}$$

with the inverse Langevin function $\mathcal{L}^{-1}(x)$ replaced by the Padé approximation (Cohen, 1991)

$$\mathcal{L}^{-1}(x) = x \frac{3 - x^2}{1 - x^2} \tag{22}$$

and the mean chain stretch λ_C simplifies under uniaxial stress and isochoric deformation to

$$\lambda_C = \sqrt{\frac{\operatorname{tr} \left[\boldsymbol{\lambda}^{f\,2} \right]}{3}} = \sqrt{\frac{1}{3} \left(\lambda^{f\,2} + \frac{2}{\lambda^f} \right)} \, . \tag{23}$$

Eq. (21) involves two material parameters, namely the initial shear modulus $\mu_{f,\mathrm{EC}}$ and the limit stretch λ_L corresponding to the entanglement density of the glassy polymer. An additional nonlinear spring in series to the dashpot (Fig. 3, element B) is included to enable a realistic response upon instantaneous loading. The stress is given by an incompressible neo-Hookean material model

$$\sigma_{\mathrm{NH}}^f = \mu_{f,\mathrm{NH}} \left(\lambda^{e\,2} - \frac{1}{\lambda^e} \right) , \tag{24}$$

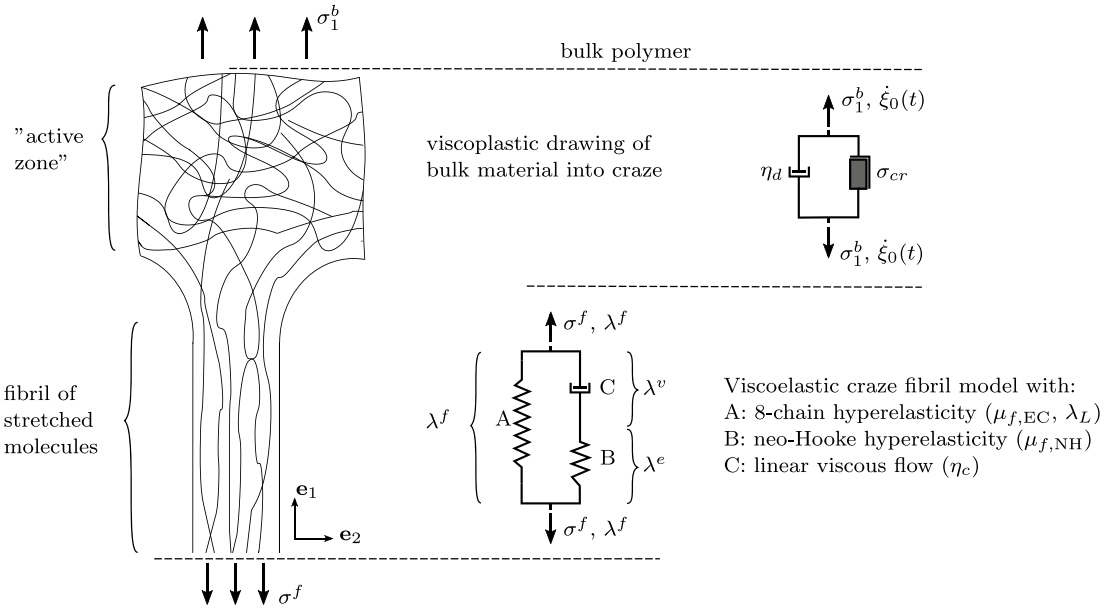

Fig. 3. Fibril model comprising viscoplastic drawing from the active zone and viscoelastic fibril deformation.

which introduces a second shear modulus $\mu_{f,\mathrm{NH}}$ as a material parameter. The viscous fibril deformation is described by the flow rule

$$\dot{\lambda}^v = \frac{2}{3\,\eta_c}\sigma^f_{\mathrm{NH}}\lambda^v\,. \tag{25}$$

Fig. 3 illustrates the arrangement of rheological models of viscoelastic fibril deformation and viscoplastic fibril drawing. For further details on the craze model and particularly a motivation and discussion of various constitutive assumptions, e.g. the simplified linear flow models with constant viscosities in (15) and (25), the reader is referred to Laschuetza and Seelig (2024).

2.4. Remarks on parameter calibration

We aim to obtain a generic, yet representative craze response for glassy polymers. This presents the challenge that craze and bulk parameter scopes are not independent as they should describe the same (generic) material. Unlike the bulk parameters, which can be calibrated from experiments, the craze parameter calibration is difficult due to the small length scale. We address this issue in several steps to obtain a physically plausible parameter scope of the craze parameters:

First, we take bulk model parameters from the literature (cf. Appendix B), which are representative for glassy polymers. This yields the shear modulus μ_b and the Poisson's ratio ν_b for an elastic bulk material (cf. Section 3) and additionally the initial shear yield strength s_0 for an inelastic bulk material (cf. Section 4).

Second, we normalise the craze parameters with μ_b and s_0 where applicable. With the known bulk parameters, the craze model encompasses ten additional constants as well as the primordial thickness h_0. We normalise the two characteristic times $\tau_d = \eta_d/\mu_b$ and $\tau_c = \eta_c/\mu_b$, which describe the fibril drawing and the fibril creep behaviour of the craze element, respectively, with a characteristic loading time T_0 into the two dimensionless parameters τ_d/T_0 and τ_c/T_0. The geometry of the boundary value problem in Section 3 is scaled with h_0 and the primordial thickness is set to $2h_0 = 1\mu\mathrm{m}$, which is comparable to previous continuum modelling (Sharma et al., 2008). The primordial thickness can be understood as a material property which is determined by the (measurable) extension ratio and the (measurable) fibril length (craze opening displacement) at failure ($\chi_0 = 0$) according to (1).

Third, we use experimental and numerical findings from the literature to deduce representative values for the extension ratio λ_c^*, the craze initiation stress σ_{cr}^0, the saturation drawing stress σ_{cr}^* and the two viscosities η_d and η_c: The extension ratio λ_c^* has been extensively studied in experiments and $\lambda_c^* \approx 2$ is representative of the bulk parameters in Table B.2 (cf., e.g., Donald and Kramer, 1982). Craze initiation is taken to occur at a representative stress magnitude for glassy polymers, given by $\sigma_{cr}^0/\mu_b = 0.11 \approx 1.2 s_0/\mu_b$. We set the saturation drawing stress to $\sigma_{cr}^* = 2\sigma_{cr}^0/3$, which corresponds to $\sigma_{cr}^* \approx 0.8 s_0$ as used in Estevez et al. (2000). This facilitates later comparisons under monotonic loading. With set σ_{cr}^0, the fibril drawing viscosity η_d significantly influences the crack propagation speed and hence, the macroscopic stress in the far field. Linear elastic fracture mechanics is used to estimate a far field stress as experimentally observed for the mode I boundary value problem outlined in Section 3. The considered range of values for τ_d/T_0 and τ_c/T_0 is given in Section 3.1 after the boundary value problem has been presented.

Fourth, we employ molecular dynamics (MD) simulations to obtain the parameter scope for the remaining parameters, including the elastic fibril properties $\mu_{f,\mathrm{EC}}$ and $\mu_{f,\mathrm{NH}}$, the limit stretch λ_L, the parameter β_c controlling fibril jamming and the fraction α upon which mature fibrils exist. MD simulations complement well the micromechanical approach by providing insight into microscale mechanisms that are otherwise challenging to access experimentally due to their small length scale. The details of the non-standard molecular dynamics calibration are presented in Appendix A, with key considerations summarised as follows: The elastic part of the constitutive craze fibril model (cf. Fig. 3) is fitted to the stress–strain response of the MD simulations, yielding $\mu_{f,\mathrm{EC}}$, $\mu_{f,\mathrm{NH}}$ and λ_L. The parameter scope is further assessed by normalising the quantities with the MD bulk stiffness μ_b, leading to $\mu_b/\mu_f \approx 10$ and $\mu_{f,NH}/\mu_f \approx 0.5$, where $\mu_f = \mu_{f,\mathrm{EC}} + \mu_{f,\mathrm{NH}}$. According to Laschuetza et al. (2024), the fibril length in the MD simulations is closely linked to the deformation. Combined with (13), this correlation is used to determine the onset of fibril jamming as function of the craze fibril length ξ_0, resulting in $\beta_c \approx 0.15$. Similar to the idea of the morphology change depicted in Fig. 2, the MD simulations allow to determine the instant after cavitation upon which the mature craze density prevails, leading to $\alpha \approx 0.07$.

Finally, we investigate different parameter combinations to study their influence on the (generic) response.

2.5. Response of calibrated craze model

To study later the effect of μ_b/μ_f and λ_L, three materials are selected as shown in Table 1. Material 1 utilises $\mu_b/\mu_f = 1$ and a relatively high limit stretch λ_L. By contrast, material 2 takes $\mu_b/\mu_f = 10$ according to the MD findings and material 3 additionally is based on a low λ_L corresponding to the MD results.

Table 1
Material parameter sets of craze model, where s_0 and μ_b are given by the bulk material in Table B.2.

set	μ_b/μ_f	ν_b	$\mu_{f,NH}/\mu_f$	σ^0_{cr}/μ_b	$\sigma^0_{cr}/\sigma^*_{cr}$	λ^*_c	α	λ_L	β_c	$2h_0$ [μm]
1	1	0.38	0.5	$1.2s_0/\mu_b$	1.5	2	0.07	2	0.15	1
2	10	0.38	0.5	$1.2s_0/\mu_b$	1.5	2	0.07	2	0.15	1
3	10	0.38	0.5	$1.2s_0/\mu_b$	1.5	2	0.07	1.2	0.15	1

Following the study in Laschuetza and Seelig (2024), the evaluation of the three materials under uniaxial deformation in a strain controlled bilinear cyclic loading programme is depicted in Fig. 4. The characteristic loading time T_0 is set to the reciprocal of the overall deformation rate $T_0 = 1/\dot{\bar{\lambda}}_1$. All three materials exhibit qualitatively similar traits: an initial peak stress followed by a transition to a constant drawing stress plateau, while during unloading fibrils are stress-free and loose hanging until fibril jamming occurs. Notably during reloading in the 2nd cycle, material 1 shows the most pronounced hysteresis and fibril creep recovery while the fibrils are stress-free, which is represented by the offset between unloading and subsequent reloading in the next cycle (cf. magenta marking in Fig. 4 for material 1). Except for the curvature of the unloading–reloading curves, material 2 and 3 behave very similar during cyclic loading. We conclude that the change in stiffness μ_b/μ_f exhibits the most pronounced influence on the results and thus, we use material 2 as the base case in the subsequent study unless indicated otherwise.

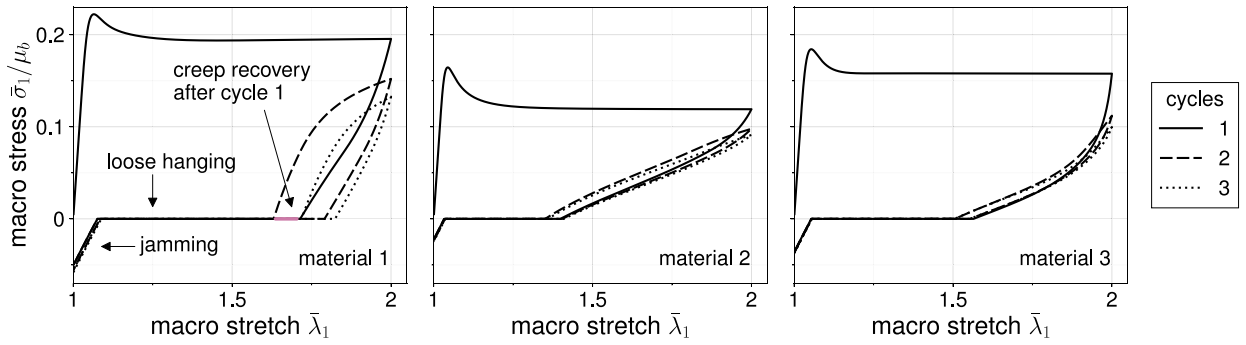

Fig. 4. Uniaxial strain response of continuum-micromechanical craze model for three consecutive loading cycles and materials outlined in Table 1. ($\tau_c/T_0 = 0.1$, $\tau_d/T_0 = 0.1$).

2.6. Numerical aspects

The craze model is defined by a system of differential algebraic equations and implemented as a user material subroutine in the finite element programme Abaqus (ABAQUS, 2023). To compute the tangent directly within the Newton–Raphson scheme, the Fortran implementation employs *dual number automatic differentiation*. To that end, we extended the dual number automatic

differentiation tool developed by Yu and Blair (2013) to accommodate the specific operations required in the implementation. Both, the craze model described in Section 2 and the bulk model for shear yielding outlined in Appendix B, are implemented with this methodology. This computational approach has been successfully deployed on the high-performance computing platform *bWUniCluster 2.0*, where both material models have been simultaneously applied.

3. Craze and crack growth in brittle glassy polymers

3.1. Model set-up and computational aspects

The 2D plane strain boundary value problem (BVP) of a rectangular plate with an edge crack of initial length a_0 subjected to mode I loading is depicted in Fig. 5. Loading is imposed in terms of a displacement controlled bilinear cyclic loading programme $u_y(t, T, R_u)$ with time t, period T, displacement velocity $\dot{u}_y$ and load ratio $R_u = u_{y,min}/u_{y,max}$ as sketched in Fig. 5(b). The notch tip radius $r_t = 50h_0$ (see Fig. 5(c)) is introduced to alleviate mesh distortions and the r_t magnitude is comparable to Estevez et al. (2000), Estevez and van der Giessen (2005). Mode I symmetry is exploited and one layer of craze elements with initial thickness h_0 is placed along the ligament indicated by the red line in Fig. 5. All length dimensions scale with the primordial thickness h_0. The BVP is solved with the commercial finite element (FE) software Abaqus/Explicit (ABAQUS, 2023) to properly capture dynamic effects during potentially unstable crack growth. In contrast to various other studies, e.g. Tijssens et al. (2000a), Estevez et al. (2000), the occurrence of dynamic effects also has led us to avoid a small scale yielding BVP. Instead the entire specimen is modelled as shown in Fig. 5(a). Both, craze and bulk material are implemented as user material subroutines and craze elements are removed once the failure criterion of a critical craze thickness $\xi_0 = \xi_{0,\max}$ is met (cf. (16)). Elements along the ligament are quadratic in shape with a dimension of h_0. The ratio $r_t/h_0 = 50$ provides an indication of the mesh resolution.[1] Since this type of BVP is prone to hourglassing, the finite elements are fully integrated.

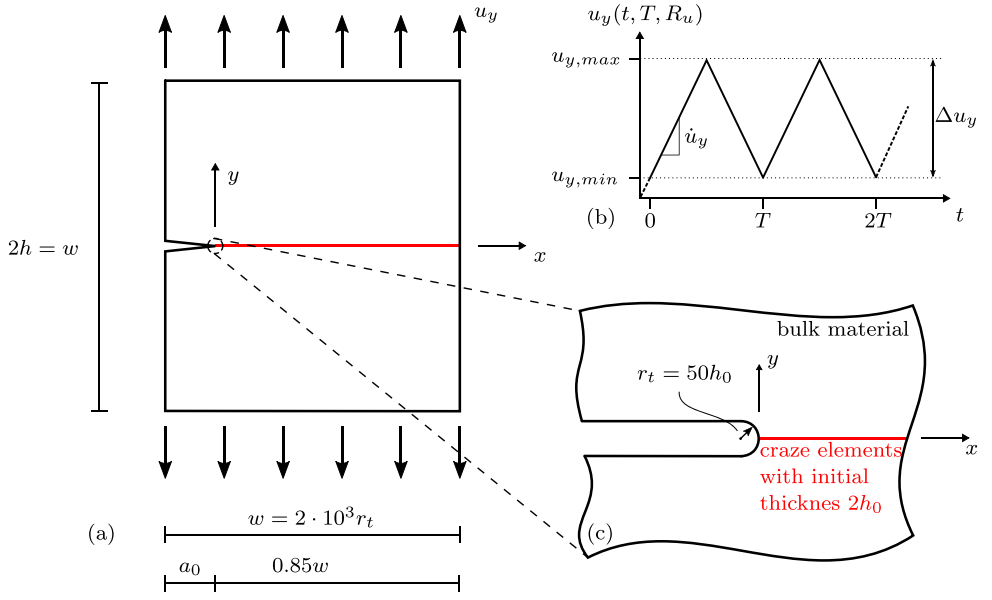

Fig. 5. (a) Mode I boundary value problem with (b) displacement controlled cyclic loading history and (c) detail of the round crack tip.

The maximum displacement $u_{y,max}$ (Fig. 5(b)) is chosen to yield a realistic far field stress as observed in experiments. With inelasticity limited to a small region around the crack tip, linear elastic fracture mechanics arguments are employed to estimate σ_y in the far field. For the current BVP, the stress intensity factor is $K_I = F\sigma_y\sqrt{\pi a_0}$ with a shape factor $F \approx 0.9$ according to table C10.15 in Fett (2008). We consider two cases: one for an elastic and one for an inelastic bulk material. In the case of a purely elastic bulk response, the fracture toughness of glassy polymers typically ranges around $K_{Ic} \approx 1\text{MPa}\sqrt{\text{m}}$. This yields a realistic far field stress $\sigma_y \approx 7.5\text{MPa}$. The magnitude for more ductile glassy polymers is deduced from experiments where both crazing and shear yielding take place. According to Takemori (1990), crack tip plastic zones involving a strong interaction of both mechanisms in PC occur in the range of up to $\Delta K_I = 1.3\text{MPa}\sqrt{\text{m}}$ for $R = F_{min}/F_{max} = 0.1$. This leads to $\sigma_y \approx 10.5\text{MPa}$ as far field stress.

The fibril drawing viscosity η_d is chosen so that crack initiation does not take place in the first cycle while, on the other hand, avoiding a fatigue loading regime where thousands of cycles are necessary. To compare varying loading periods T due to, for instance, different R_u, the reciprocal of the strain rate in the far field is used as characteristic time $T_0 = h/\dot{u}_y$. This results in

[1] The FE mesh is visible in Fig. 6, showing the situation at some instant after crack initiation.

$\tau_d/T_0 \approx 10^{-4}$. We remark that the small value arises from the choice of the far field velocity. Rescaling with the ratio of specimen height and primordial thickness $h/h_0 = 5 \cdot 10^4$ yields $\tau_d/T_0 \approx 5$, which is more comparable to the values given in Fig. 4. However, since the far field velocity is more representative in experiments, this rescaling is omitted. As a normalised measure of the loading magnitude, the far field strain, given by $\varepsilon_y = u_y/h$, is introduced.

In the following, the evaluation mainly focuses on quantities along the ligament. The craze length l_c is computed as the longest contiguous craze segment. That is, l_c neither includes craze sections separated by a crack nor by un-crazed elements. This method helps to focus on the evolution of the most dominant, i.e. longest, craze, which is important since crack initiation may not occur at the notch tip. On the other hand, the crack length a is calculated as the cumulative sum of all cracks, i.e. including separated crack sections.

3.2. Numerical results

We first study the situation of a purely linear elastic bulk material with craze material 2 (cf. Table 1) and corresponding elastic bulk parameters μ_b and ν_b. Cyclic loading with $R_u = 0$ and $\epsilon_{y,max} = 2.5 \cdot 10^{-3}$ is considered, resulting in an average far field stress of $\sigma_y \approx 7.6$MPa. If not indicated differently, the normalised drawing and fibril creep viscosities are taken as $\tau_d/T_0 = 5 \cdot 10^{-4}$ and $\tau_c/T_0 = 10^{-4}$, respectively.

Fig. 6 presents a snapshot of the vertical stress field σ_y along with the finite element mesh close to the notch tip at peak load in the 31st cycle some time after crack initiation. As annotated in Fig. 6, the stress distribution exhibits a double peak at the crack tip and at the craze tip. The craze extends between those peaks, while elements on the right-hand side of the craze tip have not yet initiated.

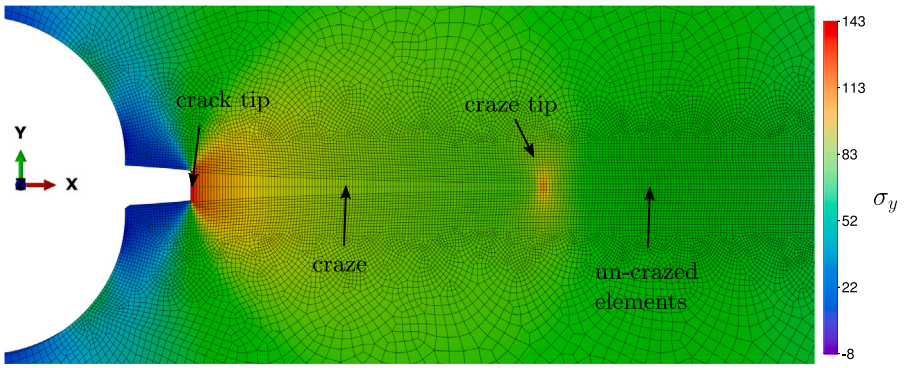

Fig. 6. Stress field σ_y at the notch tip at peak load in the 31st cycle.

The stress distribution and the craze opening contour in terms of the fibril length are shown at four instants throughout the 31st cycle in Fig. 7 during loading (black line), at peak load (magenta line), during unloading (green line) and at overall zero displacement (orange line). As the elements on the right-hand side of the craze tip have not yet initiated, they still exhibit elastic bulk behaviour, resulting in a quasi-identical stress distribution in stage 1 and stage 3 (Fig. 7(a)). The double stress peak is visible in instant 2, where the stress at the crack tip exceeds the stress at the craze tip.

In contrast, in stages 1 and 3 the stress at the craze tip is higher than at the crack tip. Moreover, the stress at the crack tip during loading (black line) is higher than during unloading (green line), despite the smaller craze width (cf. Fig. 7(b)). This effect is

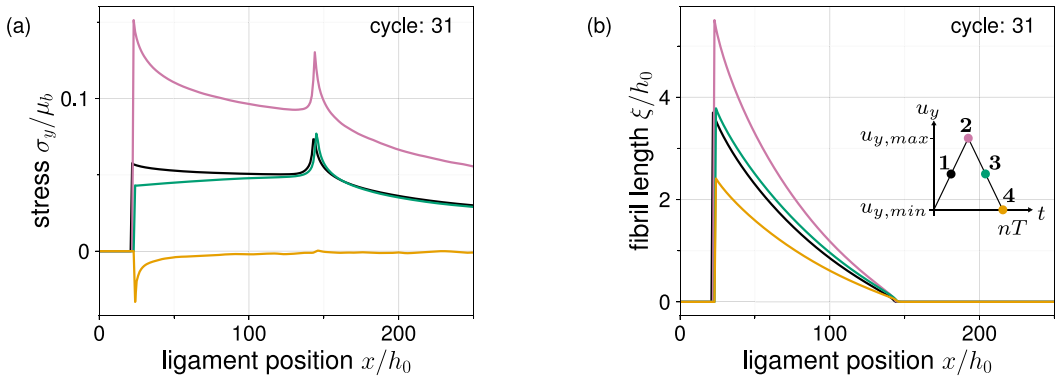

Fig. 7. (a) Normalised stress distribution and (b) craze contour in terms of normalised fibril length along ligament at four loading stages.

attributed to the elongation of the craze fibrils due to drawing and creep deformation throughout the loading cycle. The relatively constant shift in the craze contour between stage 1 and 3 (Fig. 7(b)) suggests uniform drawing along the craze. In contrast, creep deformation depends on the current (relaxed) fibril length ξ_0 and becomes more dominant for longer fibrils (cf. Laschuetza and Seelig, 2024), as prevailing at the crack tip. Consequently, the deviation in crack tip stress between instant 1 and 3 is attributed to the fibril creep viscosity. Instant 4 displays the influence of fibril jamming, which is again most pronounced at the crack tip where ξ_0 reaches its maximum value. The slight horizontal shift of the stress curves throughout the cycle indicates the small amount of crack propagation.

The influence of the fibril creep viscosity η_c on the ligament stress and the evolution of the craze and crack length is studied over a range of four orders of magnitude of the dimensionless parameter τ_c/T_0 in Fig. 8. Higher τ_c/T_0 values enhance fibril stiffness, resulting in higher stress, which is most pronounced at the crack tip with the longest craze fibrils ξ_0 (cf. Fig. 8(a)). In all cases, craze initiation occurs at the notch tip at 40% of the peak load during the first loading cycle. Thereafter, the craze length l_c monotonically grows over multiple cycles prior to failure, representing cyclic damage accumulation (cf. Fig. 8(b)). The inset in Fig. 8(b) illustrates that craze growth is interrupted by arrest phases during unloading. Crack initiation also takes place at the notch tip and is delayed from the 17th to the 23rd loading cycle as τ_c/T_0 decreases. The correlation between σ_y and τ_c/T_0 results in a faster crack propagation after initiation, whereas the craze length l_c shortens with increasing τ_c/T_0.

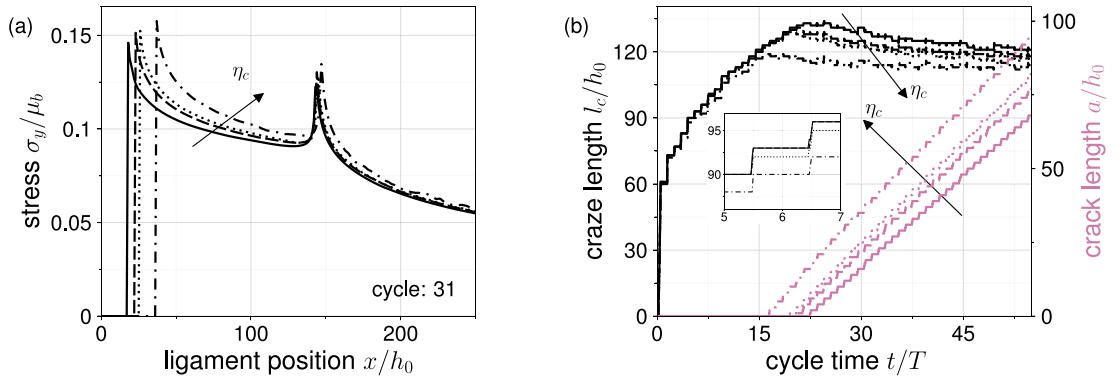

Fig. 8. Influence of fibril creep viscosity in terms of $\tau_c/T_0 = [10^{-5}, 10^{-4}, 10^{-3}, 10^{-2}]$ on (a) stress distribution along ligament at peak load and on (b) temporal craze length and crack length evolution with a zoom.

The influence of the loading magnitude is analysed by increasing the overall deformation by 20% in Fig. 9, allowing for comparisons with experimental findings discussed below. The craze contour at peak load in cycles with approximately equal crack extensions is shown in Fig. 9(a). The evolution of the craze and crack length during the cyclic loading history is depicted in Fig. 9(b). The craze width at the crack tip $\xi(x = a)$, the craze length l_c and the crack growth rate all increase with Δu_y. However, the most notable difference is the change in the evolution of l_c, which exhibits a more pronounced variation for the higher loading amplitude.

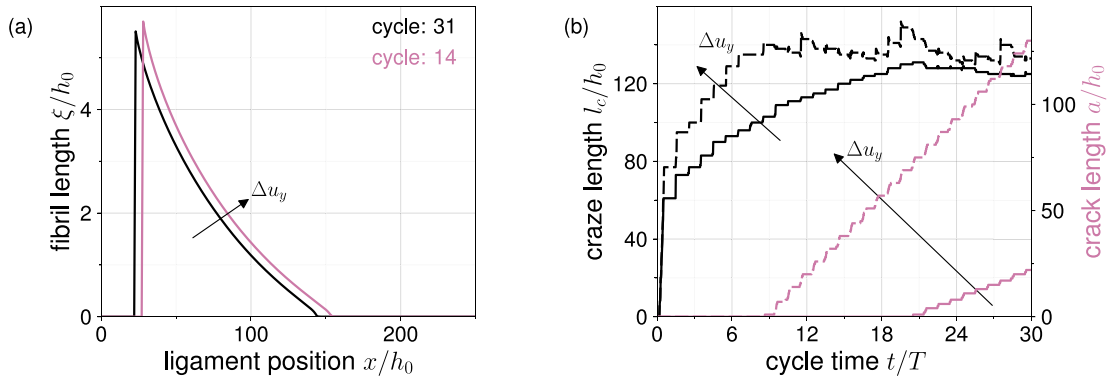

Fig. 9. Influence of load increase by 20% on (a) craze contour and (b) craze and crack length evolution.

3.3. Discussion

The simulation results, including the parameter choice, are assessed by drawing comparisons to experiments and previous numerical analyses from the literature. The double stress peak at the crack tip and the craze tip is in accordance with previous results for various brittle glassy polymers, e.g. in Wang and Kramer (1982), Bevan et al. (1986), Ungsuwarungsri and Knauss (1988), Pulos and Knauss (1998), who calculated the normal stress distribution along a craze based on experimentally measured craze opening

contours and the assumption of a linear elastic bulk response. A non-proportional stress redistribution along a craze during a loading-unloading cycle similar to Fig. 7(a) is also reported in Pulos and Knauss (1998). In addition, the stress profile at unloading computed in Bevan et al. (1986) shows a compressive stress at the crack tip and a slight tensile stress at the craze tip, which corresponds to the possible effect of fibril jamming at the unloaded crack tip and agrees well with our result (orange line) in Fig. 7(a). A further quantity which has been studied extensively is the craze profile, from which characteristic ratios of craze length vs. craze opening displacement $l_c/(2\xi_{max})$ can be derived. A representative range for glassy polymers is $l_c/(2\xi_{max}) = 10 - 20$, cf. Döll and Könczöl (1990), while the results here yield $l_c/(2\xi_{max}) \approx 11.3$, which is well within the experimental range. We remark, however, that this ratio is influenced by the choice of craze parameters, for instance, $\lambda_c^* = 3$ yields $l_c/(2\xi_{max}) \approx 14$. Finally, increasing the loading amplitude results in an increase in craze length l_c and craze opening displacement at the crack tip $\xi(x = a)$ due to the modelled viscosities, which also aligns with experimentally observed trends (Könczöl et al., 1990).

4. Interaction between crazing and shear yielding in ductile glassy polymers

4.1. Modelling aspects

In the following, we study the interaction of crazing and shear yielding under cyclic mode I crack growth as it may occur in more ductile glassy polymers. This extends the work by Van der Giessen and co-workers who considered monotonic loading conditions (Estevez et al., 2000; Estevez and van der Giessen, 2005). The objective far field stress outlined in Section 3.1 is obtained by the maximum deformation $\varepsilon_{y,max} = 3.3 \cdot 10^{-3}$, resulting in an average far field stress of $\sigma_y \approx 10$MPa in the simulations. Additionally, following the cyclic loading conditions outlined by Takemori (1990), the load ratio is set to $R_u = 0.1$. This load ratio enables to exploit mode I symmetry, as it mitigates the effect of crack closure due to compression at the crack tip resulting from the crack tip plastic zone (cf. Rice, 1967). The viscoplastic behaviour of the bulk material is described by a modified version (Hempel, 2016) of the standard glassy polymer model by Boyce et al. (1988) (see Appendix B for details). The bulk parameters, which are representative for PC, are outlined in Table B.2. The analysed craze materials in this section are given in Table 1 and the drawing and fibril creep viscosities are taken as $\tau_d/T_0 = \tau_c/T_0 = 10^{-4}$. This choice, in conjunction with the nonlinear Eyring-type viscosity of the bulk model (cf. Appendix B), guarantees that in the following numerical studies, focusing only on a generic glassy polymer, all inelastic mechanisms (fibril drawing and creep as well as bulk shear yielding) are active.

4.2. Numerical results

At first, craze material 2 (cf. Table 1) is investigated. The field output for the accumulated plastic strain γ^p, i.e. the plastic zone, is displayed in Fig. 10 for three instants in the first cycle: just prior to craze initiation (Fig. 10(a)), after craze initiation (Fig. 10(b)) and at load maximum (Fig. 10(c)). All instants fall within the first (monotonic) loading stage, allowing for comparisons with previous work (Estevez et al., 2000). The grey area along the ligament shows the location of the un-crazed elements, while the black area indicates craze elements after initiation, i.e. $\xi_0 > 0$, and therefore the craze length l_c. The following is notable: Craze initiation, occurring at $\varepsilon_y \approx 0.4\varepsilon_{y,max}$, is preceded by shear yielding (cf. Fig. 10(a) and (b)). Although the overall plastic zone is still small in size and magnitude (cf. Fig. 10(b) and (c)), craze initiation takes place at an approximately 20% higher load compared to the elastic bulk response (cf. Section 3.2). Additionally, the craze initiates ahead of the notch root at the tip of the plastic zone where the local stress σ_y attains a maximum (cf. Fig. 10(b)). Upon initiation, the craze grows in both directions, towards the notch tip and along the ligament (cf. Fig. 10(c)), while the plastic zone develops the characteristic plane strain pattern observed in experiments, e.g. Ishikawa et al. (1977), and previous simulations, e.g. Estevez et al. (2000), Estevez and van der Giessen (2005). Craze initiation ahead of a plane strain notch is consistent with experimental results in PC (Ishikawa et al., 1977; Ishikawa and Narisawa, 1983), where the craze initiated at the intersecting shear bands. Furthermore, it aligns with simulation results reported in Estevez et al. (2000), Estevez and van der Giessen (2005), where the location of craze initiation shifted from the notch tip into the bulk material with increasing craze initiation stress.

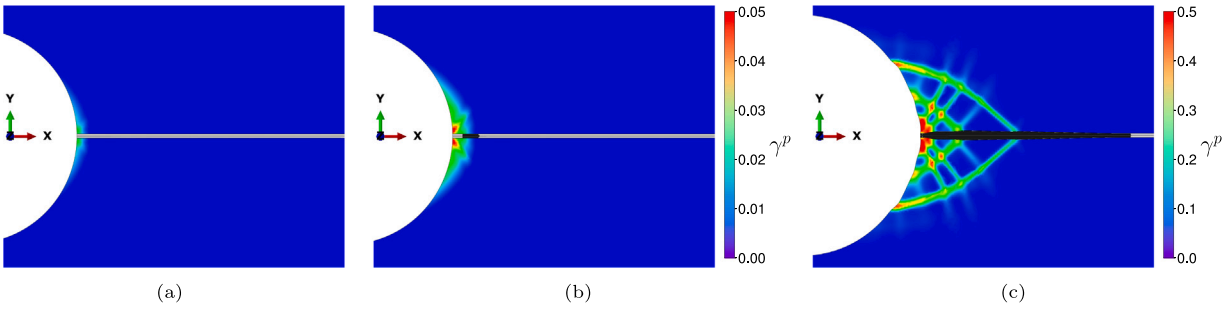

Fig. 10. Accumulated plastic strain γ^p in first cycle during loading (a) at instant prior to craze initiation, (b) at instant after craze initiation and (c) at load maximum. Black zone along ligament indicates craze. Data for craze material 2 in Table 1.

The response of craze material 2 in the course of continuous cyclic loading is analysed using snapshots of the plastic zone and craze evolution. For this, Fig. 11 displays contour plots of γ^p at three instants: after crack initiation in the 4th cycle (Fig. 11(a)) and at peak load in the 6th (Fig. 11(b)) and the 8th cycle (Fig. 11(c)). To enhance visualisation, the colour bar is capped at $\gamma^p = 1.5$, with the maximum value also indicated. After craze initiation, fibril damage accumulates over three cycles through fibril drawing, leading to craze breakdown at the outermost intersecting shear band in the 4th cycle (cf. Fig. 11(a)). To account for the Bauschinger effect in glassy polymers, the shear yielding model (cf. Appendix B) incorporates kinematic hardening, resulting in a continuous increase in the γ^p magnitude with each loading cycle. Despite the quantitative increase, the plastic zone remains qualitatively stationary after the 1st cycle (cf. Figs. 10(c) and 11(a)). With further cyclic loading, the crack propagates in both directions and connects with the notch root (cf. Fig. 11(c)). Right at the load maximum in the 6th cycle, thin shear bands form at the right-hand side crack tip (cf. Fig. 11(b)). A weaker shear band to its left forms during unloading in the 5th cycle. Both shear bands arch forward in the direction of the ligament. Each subsequent load cycle is accompanied by the formation of two additional shear bands originating from the propagating crack tip (cf. Fig. 11(c)). The first band forms at the load maximum and a second, less pronounced band during unloading, leading to the fracture pattern observed in Fig. 11(c).

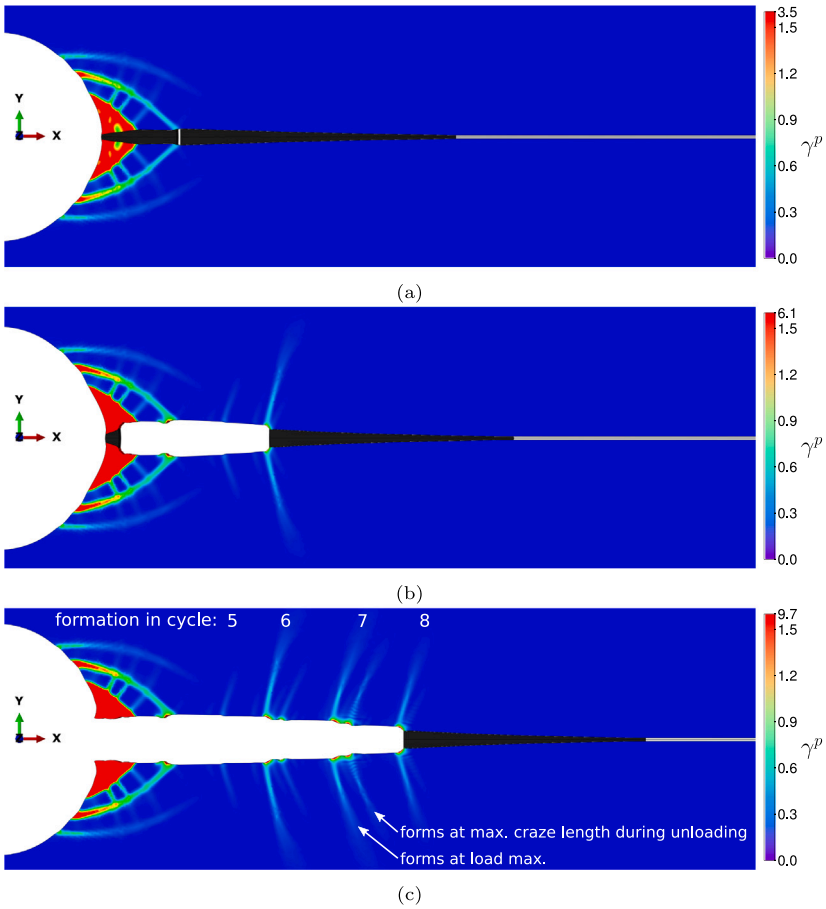

Fig. 11. Accumulated plastic strain γ^p (a) at crack initiation in cycle 4 and at load maximum in (b) cycle 6 and (c) cycle 8. Black zone along ligament indicates craze. Data for craze material 2 in Table 1.

The cyclic response is further investigated by examining the evolution of the craze length l_c and crack length a over eight consecutive loading cycles shown in Fig. 12(a) and with a detail view of the 7th cycle shown in Fig. 12(b). Fig. 12(a) is supplemented with the normalised loading programme (green line) and three vertical grey dotted lines indicating the start of craze growth during loading, the load peak and the end of craze growth during unloading in the 2nd cycle. Similar to the case of purely elastic bulk material (cf. Figs. 8(b) and 9(b) in Section 3.2), the craze length grows continuously until crack initiation. The vertical dotted lines indicate that growth of l_c is confined to a range around load maximum prior to crack initiation. However, since the lines are not equidistantly spaced, l_c increases asymmetrically with respect to $\varepsilon_{y,max}$. The craze length rapidly drops at crack initiation, primarily due to the computation methodology of l_c outlined in Section 3.1. The further decline of l_c in the 5th cycle is indeed associated with a shrinking craze zone of the right-hand side craze in Fig. 11(a). After crack initiation, the crack advances continuously with each cycle. The initial crack growth during the remainder of the 4th cycle is small, as initiation occurs during unloading. Subsequently, the crack propagates in both directions (cf. Fig. 11(b)) until it reaches the notch tip in the 7th cycle. The transition from two propagating crack tips to one combined with an initially higher crack velocity in the direction of the notch results in a large crack

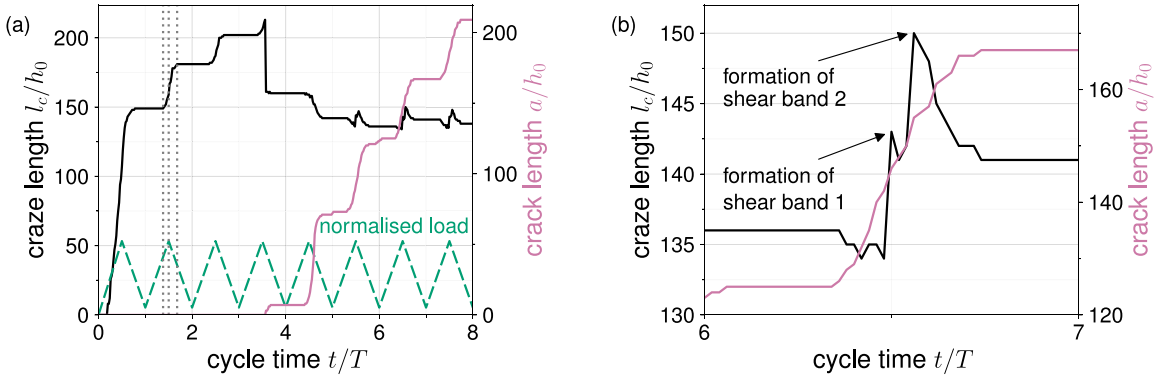

Fig. 12. Craze length (black) and crack length (magenta) evolution for (a) 8 loading cycles with normalised load (green) and (b) detailed view of 7th cycle. Data for craze material 2 in Table 1.

growth increment Δa in the 5th cycle, which thereafter declines. Throughout one cycle, l_c initially decreases while crack propagation commences (cf. Fig. 12(b)). That is, the leading edge of the craze remains stationary while the trailing edge at the crack tip advances. Coinciding with the formation of the first shear band at load maximum (cf. Fig. 11(c)), the leading edge of the craze accelerates, while the crack speed slightly declines (cf. Fig. 12(b)). The formation of the second shear band in Fig. 11(c) occurs right at the l_c peak during unloading.

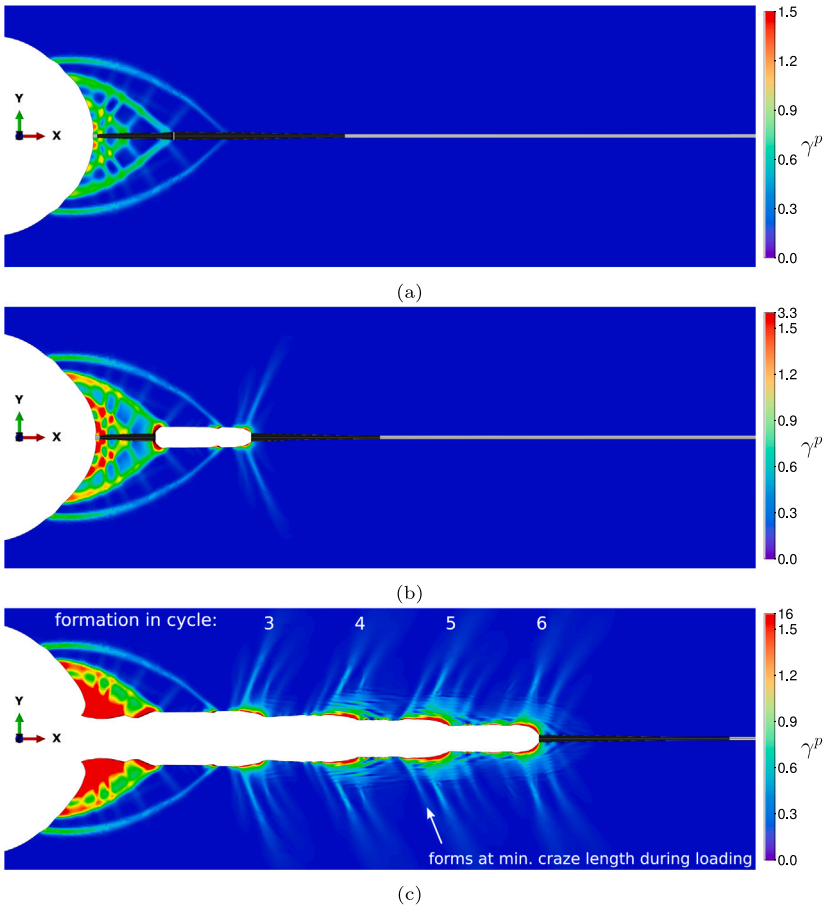

Fig. 13. Accumulated plastic strain γ^p (a) at crack initiation in cycle 2 and at load maximum in (b) cycle 3 and (b) cycle 6. Black zone along ligament indicates craze. Data for craze material 1 in Table 1.

To elucidate the role of the crack tip plastic zone on the crack and craze advancement, craze material 1 (cf. Table 1) with $\mu_b/\mu_f = 1$ is investigated in the following. With the bulk parameters remaining the same, the change in material corresponds to a higher fibril stiffness. Likewise to above, snapshots of the plastic zone and craze evolution at three instance – featuring crack initiation in the 2nd cycle and load maxima in the 3rd and 6th cycle – are shown in Fig. 13. At crack initiation, the plastic zone resembles that of the previous material (cf. Figs. 11(a) and 13(a)). Moreover, crack initiation essentially occurs at the same location. However, the higher fibril stiffness results in higher craze stress (cf. Fig. 4), leading to accelerated fibril drawing and, consequently, the earlier crack initiation in the 2nd cycle. Similarly, this leads to faster crack propagation and elevated plastic activity, resulting in a much more pronounced plastic zone depicted in Fig. 13(c).

For material 1, the quantitative evolution of the fracture process over six consecutive loading cycles is shown in Fig. 14, displaying the craze length l_c (black line) and crack length a (magenta line) with a detail view of the 5th cycle. Additionally, Fig. 14(b) includes three vertical grey dotted lines indicating the load maximum and two equidistant instants, where the left line marks the instant before the formation of a plastic zone at the current crack tip. The following traits are qualitatively similar to those of material 2: First, craze initiation is succeeded by a monotonic increase in l_c until crack initiation. Second, the crack propagates continuously in each cycle, with the largest crack increment occurring in the cycle immediately after initiation. Finally, the trailing and leading edges of the craze advance at different velocities throughout a cycle, resulting in the non-monotonic variation of l_c.

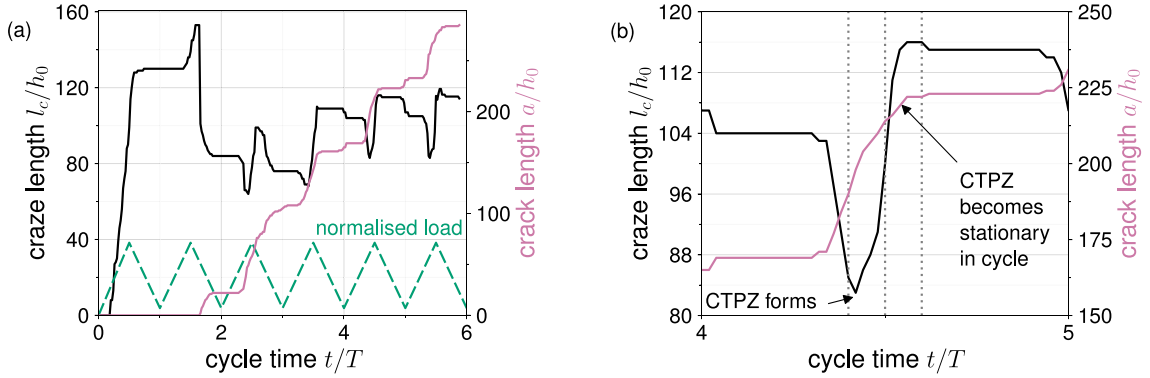

Fig. 14. Craze length (black) and crack length (magenta) evolution for (a) 6 loading cycles with normalised load (green) and (b) detailed view of 5th cycle. Data for craze material 1 in Table 1.

The role of the crack tip plastic zone can be deduced from Fig. 14(b) in combination with Fig. 15, which shows snapshots of the plastic zone for the three instants marked by the vertical lines in Fig. 14(b). Crack growth starts at $\varepsilon_y = 0.64\varepsilon_{y,max}$ and is primarily confined to the loading stage (i.e. $t/T < 4.5$). The crack propagates initially into an elastic medium (cf. Fig. 15(a)) and without energy dissipation of the bulk, the crack growth is comparatively fast. However, it significantly slows down once a crack tip plastic zone (CTPZ) develops in form of shear bands during loading at $\varepsilon_y = 0.84\varepsilon_{y,max}$, coinciding with the minimum craze length in Fig. 14(b). The plastic zone continues to develop (cf. Fig. 15(b)), while crack growth slows down. Simultaneously, l_c rapidly increases from $83h_0$ to $116h_0$, corresponding to a rise of approximately 40% in craze length. Just preceding crack arrest, the crack tip plastic zone becomes stationary and maintains the shape in Fig. 15(c). The crack arrests during unloading at a load level of $\varepsilon_y = 0.76\varepsilon_{y,max}$, which is nearly 20% higher than the load that initiated crack growth in that cycle. The pronounced plastic zone prior to $\varepsilon_{y,max}$ and the delayed crack growth behaviour is in contrast to material 2 (cf. Figs. 11 and 12(b)). Hence, we conclude that the crack tip plastic zone impedes significantly the crack advance.

To investigate the driving mechanism behind the observed delayed crack propagation, the craze contour is shown in Fig. 16(a) for material 2 and in Fig. 16(b) for material 1 at equidistant time intervals of $\pm 0.1\Delta t/T$ around peak loading at the indicated

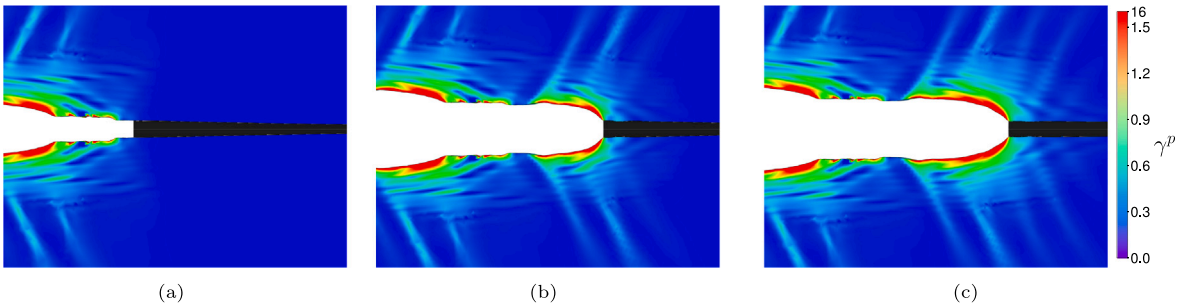

Fig. 15. Detail of crack tip plastic zone in 5th cycle (a) instant just prior to crack tip plastic zone formation at $t/T = 4.4$, (b) at peak load $t/T = 4.5$ and (c) during unloading at $t/T = 4.6$. Vertical lines in Fig. 14(b) indicate instants. Black zone along ligament indicates craze. Data for craze material 1 in Table 1.

load cycle. Note that for material 1 (Fig. 16(b)), these time instants correspond to the snapshots in Fig. 15 and the vertical lines in Fig. 14(b). The following trends apply to both materials but are much more pronounced for material 1 (Fig. 16(b)): Prior to crack tip plasticity (black lines), the craze width monotonically declines from the crack tip. Once the crack tip plastic zone forms, the craze contour exhibits a locally confined plateau at the crack tip (magenta and green lines). This plateau corresponds to a plasticity-induced local unloading of the craze fibrils, which impedes crack propagation. Further fibril growth is necessary before additional crack advancement can occur, which is enabled by the increase in craze length l_c seen in Fig. 14(b). The plateau is most pronounced for the largest crack tip plastic zone (green line in Fig. 16(b)), where crack propagation is most impeded. Concluding, this analysis suggests that the delayed crack propagation results from the unloading of the crack tip due to the crack tip plastic zone. Subsequently, l_c must first grow (cf. Fig. 14(b)) to reach a critical craze width, which then permits further crack advance.

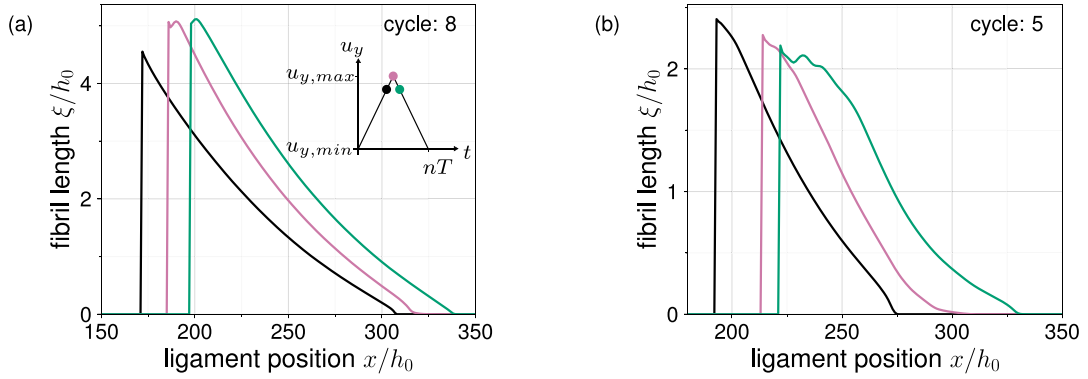

Fig. 16. Craze contour at equidistant time intervals around peak loading ($\pm 0.1\Delta t/T$) of indicated cycle for (a) craze material 2 and (b) craze material 1 for which the vertical lines in Fig. 14(b) indicate instants.

Reducing the limit stretch λ_L in the craze model so it aligns with the MD results (cf. material 3 in Table 1), yields similar results to material 2. For conciseness, results are therefore only presented and briefly discussed in Appendix C.

4.3. Discussion

The name-giving shape of the *epsilon crack tip plastic zone* where shear bands and a craze emanate from the crack tip was reported by Mills and Walker (1980) and extensively studied by Takemori, e.g. Takemori and Kambour (1981), Takemori (1990), in the context of *discontinuous crack growth* under cyclic (fatigue) loading. The formation of shear bands increases the load bearing capacity, which Takemori (1990) attributed to a shielding of the craze by reducing the hydrostatic stress. The simulation results (cf. Figs. 11 and 13) exhibit qualitative similarity to those presented in Fig. 2 and Fig. 15 of Takemori (1990). In both cases, shear bands initiate at the crack tip and arch towards the craze. Moreover, the craze length varies in the course of crack propagation which is a feature also observed in discontinuous crack growth. However, unlike the experimental observations, our simulations show *normal crack growth*, i.e. the crack propagates in each cycle and additionally the craze length varies throughout one cycle. Nonetheless, a noteworthy similarity is observed in the *delayed crack propagation* once a pronounced plastic zone forms. The mechanisms driving this crack deceleration and potential arrest are attributed to local crack tip plasticity-induced unloading. This provides a physical explanation for the delaying crack propagation, which may be extended to discontinuous crack growth.

For materials with less crack tip plasticity, such as material 2, the simulation results align well with the experimental picture obtained from measuring fatigue striations as discussed in the review (Döll and Könczöl, 1990). In these cases, the crack advances predominantly near the load maximum. Moreover, the crack growth precedes craze growth, so that the crack initially propagates into the stationary craze (cf. Fig. 12(b)). Once crack and craze growth arrests, the craze length returns approximately to its initial length at the beginning of the cycle (cf. Fig. 12(a)). Yet, the simulations provide additional insights, showing that the craze length rapidly increases and ceases to grow *before* the crack arrests.

5. Concluding remarks

Craze and crack propagation in glassy polymers under cyclic mode I loading were investigated numerically by employing a recently developed continuum-micromechanical model for crazing. A particular challenge was the parameter calibration, as craze and bulk parameters need to be chosen consistently to yield a generic, but representative glassy polymer response. To address this, the bulk model parameters were based on a glassy polymer calibration from the literature. Subsequently, the craze parameters were normalised with the bulk parameters accordingly. Parameter scopes of the craze model, which cannot be obtained from the experimental literature, were identified using molecular dynamics simulations of the cyclic craze response.

Two types of craze and crack growth simulations were conducted, namely in brittle and in ductile glassy polymers. The craze model reproduces important craze characteristics from the experimental literature for brittle glassy polymers. This includes measurements such as the ratio of craze length to craze width, the craze contour and experimental trends, for instance, the increased crack opening displacement and craze width with higher load amplitudes due to the modelled viscosities. Moreover,

similar to experimental findings on *normal fatigue crack growth*, both, crack and craze, grew near load maximum and arrested during unloading. The simulation results also aligned with previous experimental and theoretical results, indicating a double stress peak at the crack and craze tips and compression at the crack tip during unloading. Additionally, building upon work by Van der Giessen and co-workers (Estevez et al., 2000), the competition of crazing and shear yielding under cyclic loading for ductile glassy polymers was analysed. The presence of a plastic zone was found to increase the load for craze initiation and, in accordance with experiments (Ishikawa et al., 1977) and previous simulations (Estevez et al., 2000), craze and crack initiation occurred ahead of the notch root. The plastic zone exhibited similarity with the epsilon crack tip plastic zone observed in cyclic (fatigue) loading. The model replicated the initiation of shear bands at the current crack tip, which grew and arched towards the craze. A salient finding of this study was the delayed crack propagation due to crack tip plasticity. This delay was attributed to plasticity-induced unloading of the craze adjacent to the crack tip, which required additional craze growth prior to further crack advance. The size of the unloaded area, influencing the delay, correlated to the amount of crack tip plasticity.

The study faces some limitations: First, the results were obtained using a generic glassy polymer and hence, limiting the results to qualitative assessment. Second, the simulations do not yet capture the so-called *discontinuous* or *retarded* crack growth, where the crack advances by jumps after remaining stationary for hundreds of loading cycles. It is hypothesised that thermal fatigue of the craze fibrils in close vicinity to the crack tip might influence this behaviour (cf., e.g., Döll and Könczöl, 1990). We, on the other hand, considered only isothermal conditions. However, insights from experiments and molecular dynamics suggest a hysteretic craze response. The associated dissipation could be a source of heating and hence, adiabatic or coupled thermo-mechanical simulations could offer valuable insight. Yet, this approach presents significant challenges as it demands accurately determining the mechanical response of crazes at elevated temperatures.

Concluding, an interesting direction for future work appears to be experimental investigations of the cyclic craze response. An emphasis on the cyclic uniaxial craze behaviour across various strain rates and temperatures will be of great value. This data can contribute to (in-)validate the molecular dynamic results, which would help with additional physically motivated model refinements.

CRediT authorship contribution statement

Tobias Laschuetza: Writing – review & editing, Writing – original draft, Software, Methodology, Formal analysis, Conceptualization. **Thomas Seelig:** Writing – review & editing, Writing – original draft, Supervision, Methodology, Formal analysis, Conceptualization.

Declaration of competing interest

The authors declare that they have no known competing financial interests or personal relationships that could have appeared to influence the work reported in this paper.

Acknowledgements

We thank Jörg Rottler for the stimulating discussions. Computational support from the state of Baden-Württemberg through bwHPC is gratefully acknowledged.

Appendix A. Parameter calibration via molecular dynamics simulations of cyclic crazing

The molecular dynamics (MD) based calibration builds upon recent work (Laschuetza et al., 2024) where a generic bead–spring model was used to investigate the cyclic craze response in glassy polymers subjected to uniaxial deformation. The focus here is solely on utilising the results to estimate the material parameters. Since the MD model is standard and has been extensively used in previous craze studies (e.g. Rottler and Robbins, 2003; Ge et al., 2017), the reader is referred to Laschuetza et al. (2024) for details on model and simulation. In the following, the overall stretch and the axial stress of the MD system is denoted by λ and σ, respectively. They correspond to $\bar{\lambda}_1$ and $\bar{\sigma}_1$ of the craze model in Section 2. The loading programme, the stress response and a snapshot of the craze at peak deformation is shown in Fig. A.17. The initially isotropic glass is uniaxially deformed to a maximum stretch $\lambda_{max} = 10$ (grey dotted line in Fig. A.17(a) and in favour of visibility only partially shown in (b)), which leads to a full conversion of bulk material to fibrillated craze matter (cf. snapshot in Fig. A.17). Subsequently, the craze is subjected to a cyclic loading programme with varying unloading magnitudes $\lambda_{min} = [1, 2, 3, 5, 8]$, followed by reloading to λ_{max}. The stress response of the five independent simulations is shown in Fig. A.17(b) exhibiting a hysteresis and a reloading behaviour which depends on λ_{min}. Furthermore, it is noteworthy that the craze exhibits a pronounced compressive stress (cf. black dashed line Fig. A.17(b)) prior to reaching the macroscopic undeformed state $\lambda = 1$. This stress arises from the intermolecular resistance (cf. Laschuetza et al., 2024) and is macroscopically interpreted as fibril jamming.[2]

Additional useful information from the MD simulations is the interaction between bulk and craze material subjected to uniaxial cyclic loading. Those bulk-craze systems are created by reducing λ_{max}. Scaling the deformation in terms of the engineering strain of each system with its value at λ_{max} defines the scaled engineering strain $\varepsilon_E = (\lambda - 1)/(\lambda_{max} - 1)$. The thus rescaled stress–strain

[2] For a detailed analysis of the driving mechanisms leading to this mechanical response, the reader is referred to Laschuetza et al. (2024).

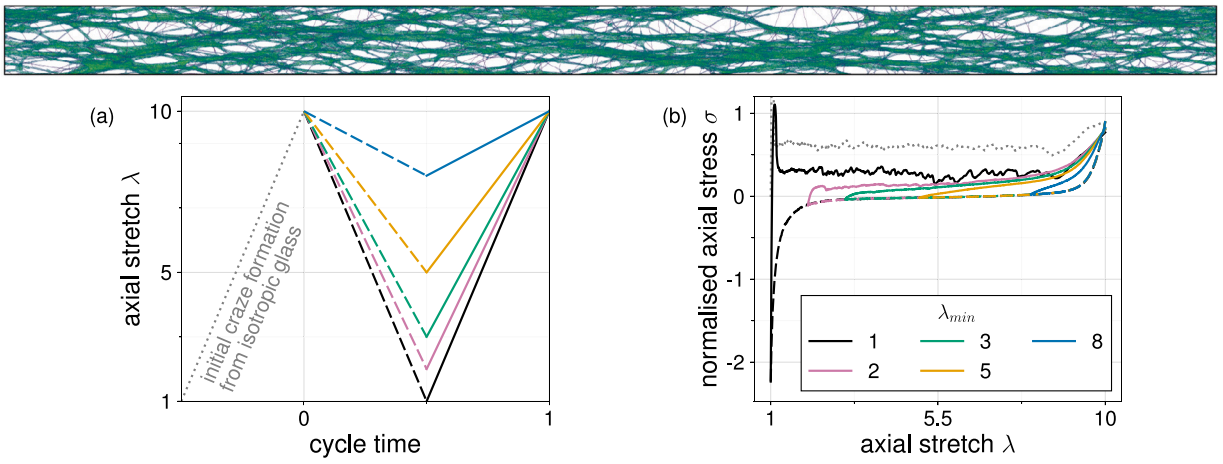

Fig. A.17. Snapshot from MD simulation for craze at $\lambda_{max} = 10$ (top) and (a) uniaxial deformation controlled cyclic loading programme with (b) stress response of sole fibrillated craze matter for five unloading magnitudes λ_{min}.

response is depicted in Fig. A.18 for sole craze matter (λ_{max}=10) and two additional bulk-craze systems. To provide a notion of the bulk-craze composition for $\lambda_{max} = 5$ and $\lambda_{max} = 2$, snapshots for the two systems at their respective λ_{max} are also displayed in Fig. A.18. An interesting observation is the quasi-collapse of the stress–strain curves, which implies a scaling of the craze response with λ_{max}. This, on the other hand, is related to the maximum fibril length as discussed in detail in Laschuetza et al. (2024) and which aligns well with the micromechanical framework of the continuum model.

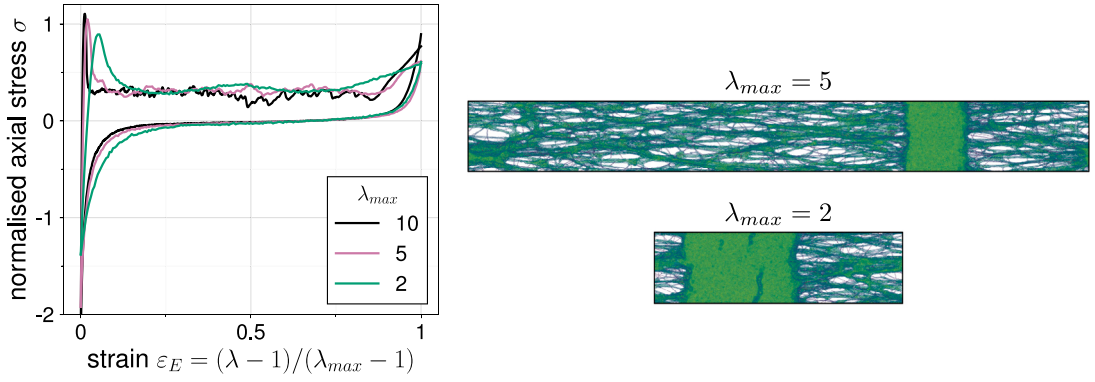

Fig. A.18. Quasi-collapse of hysteresis for several bulk-craze compositions λ_{max} when scaled to ε_E (left) and snapshots for $\lambda_{max} = [2, 5]$ (right).

Insights from Figs. A.17 and A.18 are used in the following to identify the parameters of the elastic behaviour of the fibrillated craze matter (μ_b/μ_f, $\mu_{f,NH}/\mu_f$ and λ_L), the deformation at which fibril jamming occurs during unloading (parameter β_c in (13)) and the fraction upon which mature fibrils exist (parameter α in Fig. 2).

A.1. Elastic craze fibril parameters: μ_b/μ_f, $\mu_{f,NH}/\mu_f$ and λ_L

Although λ_c^* is taken from experiments, λ_c^* from the MD simulation is needed to determine the elastic craze fibril parameters μ_b/μ_f, $\mu_{f,NH}/\mu_f$ and λ_L. Recall that λ_c describes the density-ratio in the unloaded configuration (cf. (2)). Hence, the bulk density ρ_b is taken as that of the initially undeformed isotropic glass. In contrast, the craze density ρ_c is computed at the instant $\sigma = 0$ during unloading (dashed lines in Fig. A.17(a)), which is assumed to approximately coincide with the unloaded configuration, yielding a MD based value of $\lambda_c^* \approx 6.5$. This high value is an inherent issue with the MD model, which poses challenges for transferring information from the MD model to the continuum model. This issue is addressed by normalising the MD based parameters and investigating a range of parameters associated with the elastic part of the fibril model in the continuum model (cf. Table 1).

With $\lambda_c^* \approx 6.5$, a least square fitting of the elastic craze fibril model is employed for the parameter calibration. Using only the elastic part of the craze fibril behaviour is based on the following considerations: To separate the bulk and craze response and to avoid potentially transient behaviour while bulk and craze coexist, e.g. due to fibril drawing, the cyclic MD results for sole fibrillated craze matter shown in Fig. A.17 are used as fitting data. This corresponds to the viscoelastic fibril deformation behaviour of the continuum model. Furthermore, the hysteresis in Fig. A.17(b) exhibits negligible rate dependencies as discussed in Laschuetza et al.

(2024). Combined with the inherently high deformation rates in MD simulations, we concluded that the dashpot in the craze fibril model is most appropriately taken as stiff during calibration with the MD data. This reduces the viscoelastic fibril response to the purely elastic fibril response of two springs in parallel.

For simplicity, the continuum model is fitted to the results for $\lambda_{min} = 5$, which comprises two advantages: Firstly, fibrils are assumed to be loose hanging for deformations smaller than $\lambda_c = 6.5$, which is sufficiently close to $\lambda_{min} = 5$. Secondly, $\lambda_{min} = 5$ avoids the complicated case of pore space closure for $\lambda \leq 2$, altering significantly the structural craze response (cf. Laschuetza et al., 2024). The result of the fit is shown in magenta in Fig. A.19 with one standard deviation error bars. The black lines represent the MD result already shown in Fig. A.17(b), but with the exception that the case $\lambda_{min} = 1$ is dropped to enhance visibility. The dashed line is the objective data used in the fitting. To obtain the ratio of bulk and fibril stiffness, the bulk stiffness is calculated as the secant stiffness of the glass prior to cavitation. This leads to $\mu_b/\mu_f = 10.7$, $\mu_{f,NH}/\mu_f = 0.48$ and $\lambda_L = 1.13$.

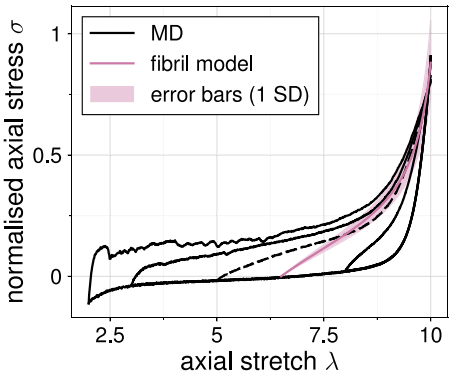

Fig. A.19. Least square fit of elastic part of craze fibril model based on MD result for $\lambda_{min} = 5$ (dashed line).

A.2. Fibril jamming: parameter β_c

Fibril jamming is observed in the MD simulations for $\lambda_{min} \leq 2$ in Fig. A.17(b) and more generally for different craze-bulk compositions below $\varepsilon_E < 0.2$ in Fig. A.18. To make use of (13), λ_{max} needs to be related to ξ_0, which is in the MD simulations the maximum attained craze length throughout deformation. Likewise to above, it is assumed that the configuration at $\sigma = 0$ during unloading closely resembles the unloaded configuration and hence, ξ_0 and χ_0 are calculated at $\sigma = 0$. Fig. A.18 is then rescaled with $\hat{\varepsilon}_1$ from (12), which defines the scaled Hencky strain $\varepsilon_H = \ln\lambda/\ln\hat{\lambda}_1$, leading to Fig. A.20. This relates the deformation to the fibril length ξ_0 and as additional benefit, it improves the collapse for $\varepsilon_H < 0.25$, which is the region of interest here.

As described in Section 2.1, fibril jamming is considered via the elastic bulk response. Therefore, it is approximated in a simplified linear manner indicated by the orange lines in Fig. A.20. The lines represent the secants connecting $\varepsilon_H = 0$ and the normalised stress $\sigma = -0.5$. Latter comprises a subjective component and was selected here due to its relevant stress magnitude with respect, for instance, to the drawing stress plateau. This results in $\beta_c \approx 0.15$, which is indicated by the black vertical marker in Fig. A.20.

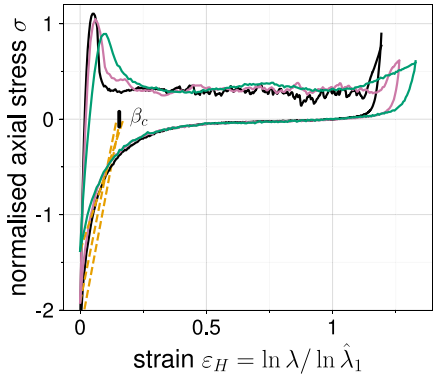

Fig. A.20. Estimation of fibril jamming parameter β_c by scaling deformation to ε_H.

A.3. Morphology change: parameter α

To identify α depicted in Fig. 2, the instant upon which mature fibrils exist during craze formation from the isotropic glass, i.e. where the density reaches $\rho_c^* = \rho_b/\lambda_c^*$, is identified. For this, the evolution of the density profile (colour coding) in axial direction (abscissa) as function of the deformation (ordinate) is shown in Fig. A.21. The initial normalised bulk density ($\rho_b \approx 1$) rapidly drops

during cavitation. As assumed in the continuum model, the MD results show that the creation of mature fibrils is a continuous process requiring further overall deformation upon cavitation. The instant $\rho = \rho_c^*$ is indicated by the black horizontal line. This configuration is then used to calculate α via the mass balance: $\alpha = 1 - \chi/h_0$, which assumes $\chi_0 \approx \chi$. For a normalised mature craze density of $\rho_c^* = 0.18$, this yields $\alpha \approx 0.07$.

Similar to experiments, a general difficulty arising from MD simulations is its statistical nature. This results in a certain subjectivity when selecting thresholds such as the craze density ρ_c^*. However, in this case, the influence of ρ_c^* is relatively insensitive as, e.g., $\rho_c^* = 0.14$ leads to $\alpha = 0.08$.

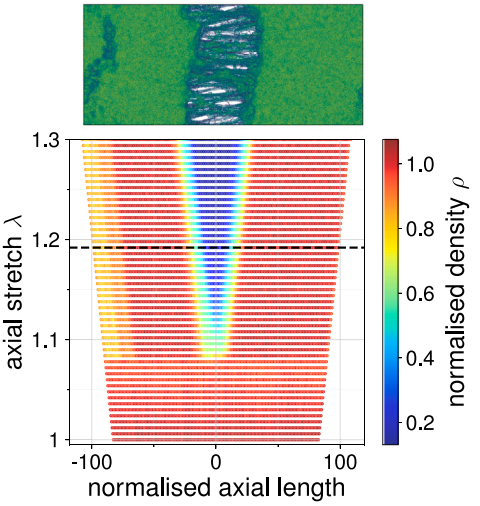

Fig. A.21. Normalised density distribution (colour coding) along axial simulation box length (abscissa) evolving with deformation (ordinate). MD snapshot at $\lambda = 1.3$ indicates local density distribution and serves to facilitate plot interpretation. Black dashed horizontal line marks instant upon which mature fibrils have formed.

Appendix B. Constitutive model for shear yielding

Building upon the early work by Boyce et al. (1988), there are well established constitutive models describing finite strain shear yielding in glassy polymers, e.g. Wu and van der Giessen (1993), Arruda et al. (1995), Anand and Gurtin (2003), Holopainen (2013), Hempel (2016). We use the version by Hempel (2016), for which the rheological model and its components are shown in Fig. B.22 and which is briefly summarised in the following.

The rheological model leads to the standard multiplicative decomposition of the deformation gradient (cf. Anand and Gurtin, 2003)

$$\boldsymbol{F} = \boldsymbol{F}^e \boldsymbol{F}^p \tag{B.1}$$

into an elastic $\boldsymbol{F}^e$ and plastic contribution $\boldsymbol{F}^p$, yielding the elastic right $\hat{\boldsymbol{C}}^e = \boldsymbol{F}^{e\mathrm{T}}\boldsymbol{F}^e$ and inelastic left Cauchy–Green tensor $\hat{\boldsymbol{b}}^p = \boldsymbol{F}^p \boldsymbol{F}^{p\mathrm{T}}$ in the intermediate (i.e. relaxed) configuration $\hat{\Omega}$. The velocity gradient $\boldsymbol{l}$ is then additively split

$$\boldsymbol{l} = \dot{\boldsymbol{F}}\boldsymbol{F}^{-1} = \boldsymbol{l}^e + \boldsymbol{F}^e \hat{\boldsymbol{l}}^p \boldsymbol{F}^{e\,-1}, \tag{B.2}$$

where $\boldsymbol{l}^e = \dot{\boldsymbol{F}}^e \dot{\boldsymbol{F}}^{e-1}$ is the elastic velocity gradient in the current configuration Ω and $\hat{\boldsymbol{l}}^p$ is the plastic component in $\hat{\Omega}$, which can be further decomposed in the symmetric rate of deformation tensor $\hat{\boldsymbol{d}}^p$ and the skew-symmetric inelastic spin tensor $\hat{\boldsymbol{w}}^p$:

$$\hat{\boldsymbol{l}}^p = \mathrm{sym}\,\hat{\boldsymbol{l}}^p + \mathrm{skw}\,\hat{\boldsymbol{l}}^p = \hat{\boldsymbol{d}}^p + \hat{\boldsymbol{w}}^p . \tag{B.3}$$

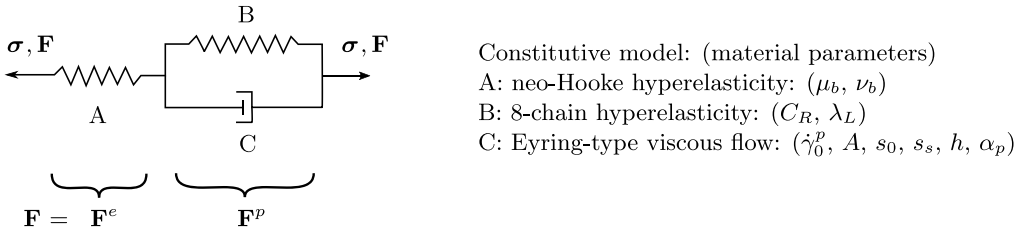

Fig. B.22. Rheological model for bulk material.

The constitutive description of the model is placed in the intermediate configuration $\hat{\Omega}$, for which the isotropic neo-Hooke hyperelasticity is given by the Mandel stress

$$\hat{\boldsymbol{\Sigma}} = \mu_b(\hat{\boldsymbol{C}}^e - \mathbf{1}) + \lambda_b\,(J^e - 1)\,J^e\mathbf{1}\,, \tag{B.4}$$

where $J^e = \det \boldsymbol{F}^e$ and which is symmetric due to the assumption that the elastic free energy contribution ψ^e and inelastic free energy contribution ψ^p are isotropic functions of $\hat{\boldsymbol{C}}^e$ and $\hat{\boldsymbol{b}}^p$, respectively. The model features the two Lamé parameters λ_b and the shear modulus μ_b. Note, as the difference is negligible for small elastic deformations, we omit correcting the elastic bulk constants due to the different elasticity models in (17) and (B.4) for the craze and bulk model, respectively.

The resistance against plastic molecular network deformation is described by the eight-chain model (Arruda and Boyce, 1993)

$$\hat{\boldsymbol{\tau}}^b = \frac{C_R\lambda_L}{3\lambda_C}\mathcal{L}^{-1}(\lambda_C/\lambda_L)\hat{\boldsymbol{b}}^{p\prime}\,, \tag{B.5}$$

where $\hat{\boldsymbol{b}}^{p\prime}$ is the deviatoric part of $\hat{\boldsymbol{b}}^p$ and λ_C is the mean chain stretch reading

$$\lambda_C = \left(\frac{\operatorname{tr}\hat{\boldsymbol{b}}^p}{3}\right)^{1/2}\,. \tag{B.6}$$

Analogous to (22), the inverse Langevin function $\mathcal{L}^{-1}(x)$ is replaced by the Padé approximation. Eq. (B.5) involves the rubber modulus C_R and the limit stretch λ_L as material parameters.

In accordance with experimental observations on shear yielding in glassy polymers, the inelastic flow is modelled incompressible, which is given by

$$\det \boldsymbol{F}^p = 1\,. \tag{B.7}$$

Furthermore, the inelastic flow in the intermediate configuration is assumed to be irrotational, i.e. $\hat{\boldsymbol{l}}^p \equiv \hat{\boldsymbol{d}}^p$, which yields the update for the inelastic deformation as

$$\dot{\boldsymbol{F}}^p = \hat{\boldsymbol{d}}^p\boldsymbol{F}^p\,. \tag{B.8}$$

To comply with the inelastic incompressibility condition in Eq. (B.7), $\hat{\boldsymbol{d}}^p$ needs to be deviatoric and hence the flow rule is constitutively prescribed as

$$\hat{\boldsymbol{d}}^p = \dot{\gamma}^p\frac{\hat{\boldsymbol{\Sigma}}^{*\prime}}{\|\hat{\boldsymbol{\Sigma}}^{*\prime}\|}\,, \tag{B.9}$$

which is a function of the deviatoric driving stress

$$\hat{\boldsymbol{\Sigma}}^{*\prime} = \hat{\boldsymbol{\Sigma}}^{\prime} - \hat{\boldsymbol{\tau}}^{b\prime}\,. \tag{B.10}$$

The inelastic shear strain rate in (B.9) is modelled by an Eyring-type flow

$$\dot{\gamma}^p = \dot{\gamma}_0^p\left(\exp\left[\frac{A}{T}\left(\|\hat{\boldsymbol{\Sigma}}^{*\prime}\| - s\right)\right] - \exp\left[-\frac{A}{T}s\right]\right)\,, \tag{B.11}$$

where $\dot{\gamma}_0^p$ and A are material parameters and T is the absolute temperature. Note, (B.11) is slightly different to the original double kink model by Argon (1973) by taking the exponent $5/6$ as 1 and by incorporating a second term which ensures $\dot{\gamma}^p = 0$ for $\|\hat{\boldsymbol{\Sigma}}^{*\prime}\| = 0$. As suggested by Boyce et al. (1988), the pressure dependence of inelastic flow and the softening upon yielding, from an initial value s_0 to a saturation value s_s, observed in polymers is incorporated via the yield strength

$$s(\gamma^p) = s_s + (s_0 - s_s)\exp\left[-\frac{h\gamma^p}{s_s}\right] - \frac{\alpha_p}{3}\operatorname{tr}\hat{\boldsymbol{\Sigma}}\,. \tag{B.12}$$

The model is implemented as a user material subroutine in the finite element programme Abaqus/Explicit (ABAQUS, 2023), which requires due to the corotational framework the corotated Cauchy stress $\boldsymbol{\sigma}_r$ as update. This is readily obtained by a push-forward operation of Eq. (B.4), defined as

$$\boldsymbol{\sigma}_r = \frac{1}{J}\boldsymbol{R}^{\mathrm{T}}\boldsymbol{F}^{e\,-\mathrm{T}}\hat{\boldsymbol{\Sigma}}\boldsymbol{F}^{e\,T}\boldsymbol{R}\,, \tag{B.13}$$

where $\boldsymbol{R}$ is the rotation tensor obtained from the polar decomposition of $\boldsymbol{F}$.

The model features 10 independent material parameters. We take the material parameters for polycarbonate (PC) at room temperature as characterised in Hund (2022) and summarised in Table B.2.

Table B.2
Material parameters of the bulk model, being representative of PC at room temperature.

μ_b/s_0	ν_b	s_s/s_0	As_0/T	h/s_0	α_p	λ_L	C_R/s_0	s_0 [MPa]	$\dot{\gamma}_0^p$ [s^{-1}]
11.3	0.38	0.6	152	0.06	1.64	1.64	0.22	82	10^{14}

Appendix C. Interaction between crazing and shear yielding for material 3

In craze material 3 (cf. Table 1), the limit stretch λ_L is reduced to align with the MD results, which constraints the overall axial extension of the craze fibril, leading to an essentially quasi-stiff fibril deformation behaviour. Compared to material 2, this changes under uniaxial deformation primarily the curvature of the unloading–reloading curve during cyclic loading (cf. Fig. 4(c)). The evolution of the craze length (black line) and the crack length (magenta line) with the normalised load programme (green dashed line) for material 3 is shown in Fig. C.23. Similar to before, the craze length grows over multiple cycles prior to crack initiation. Thereafter, the crack propagates in each cycle. Qualitatively, the results are very similar to Fig. 12(a). The key difference is the earlier onset of crack initiation in the 3rd cycle and the faster crack growth due to the stiffer craze fibril.

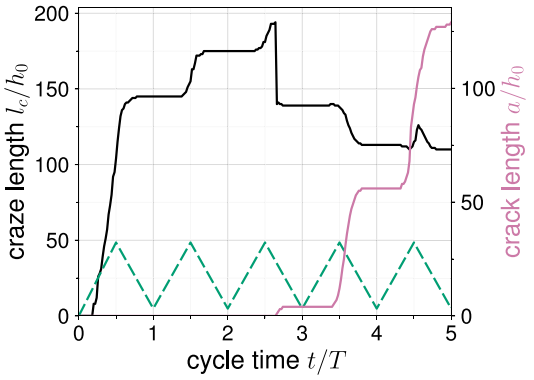

Fig. C.23. Craze length (black) and crack length (magenta) evolution with normalised load (green) for craze material 3 in Table 1.

Data availability

Data will be made available upon reasonable request from the corresponding author(s).

References

ABAQUS, 2023. Reference Manuals. Dassault Systèmes Simulia Corp, United States.

Anand, L., Gurtin, M.E., 2003. A theory of amorphous solids undergoing large deformations, with application to polymeric glasses. Int. J. Solids Struct. 40 (6), 1465–1487. http://dx.doi.org/10.1016/S0020-7683(02)00651-0.

Argon, A.S., 1973. A theory for the low-temperature plastic deformation of glassy polymers. Phil. Mag. 28 (4), 839–865. http://dx.doi.org/10.1080/14786437308220987.

Arruda, E.M., Boyce, M.C., 1993. A three-dimensional constitutive model for the large stretch behavior of rubber elastic materials. J. Mech. Phys. Solids 41 (2), 389–412. http://dx.doi.org/10.1016/0022-5096(93)90013-6.

Arruda, E.M., Boyce, M.C., Jayachandran, R., 1995. Effects of strain rate, temperature and thermomechanical coupling on the finite strain deformation of glassy polymers. Mech. Mater. 19 (2), 193–212. http://dx.doi.org/10.1016/0167-6636(94)00034-E.

Bevan, L., Döll, W., Könczöl, L., 1986. Micromechanics of a craze zone at the tip of a stationary crack. J. Polym. Sci. 24 (11), 2433–2444. http://dx.doi.org/10.1002/polb.1986.090241103.

Boyce, M.C., Parks, D.M., Argon, A.S., 1988. Large inelastic deformation of glassy polymers. Part I: Rate dependent constitutive model. Mech. Mater. 7 (1), 15–33. http://dx.doi.org/10.1016/0167-6636(88)90003-8.

Cohen, A., 1991. A pade approximant to the inverse langevin function. Rheol. Acta 30 (3), 270–273. http://dx.doi.org/10.1007/BF00366640.

Cotterell, B., 1968. Fracture propagation in organic glasses. Int. J. Fract. Mech. 4 (3), 209–217. http://dx.doi.org/10.1007/BF00185257.

Döll, W., Könczöl, L., 1990. Micromechanics of fracture under static and fatigue loading: Optical interferometry of crack tip craze zones. In: Kausch, H.H. (Ed.), Crazing in Polymers Vol. 2. In: Advances in Polymer Science, Vol. 91/92, Springer, Heidelberg, pp. 137–214. http://dx.doi.org/10.1007/BFb0018021.

Donald, A.M., Kramer, E.J., 1982. The competition between shear deformation and crazing in glassy polymers. J. Mater. Sci. 17 (7), 1871–1879. http://dx.doi.org/10.1007/BF00540402.

Estevez, R., Tijssens, M., van der Giessen, E., 2000. Modeling of the competition between shear yielding and crazing in glassy polymers. J. Mech. Phys. Solids 48 (12), 2585–2617. http://dx.doi.org/10.1016/S0022-5096(00)00016-8.

Estevez, R., van der Giessen, E., 2005. Modeling and computational analysis of fracture of glassy polymers. In: Kausch, H.-H. (Ed.), Intrinsic Molecular Mobility and Toughness of Polymers II. In: Advances in Polymer Science, Vol. 188, Springer Berlin Heidelberg, Berlin, Heidelberg, pp. 195–234. http://dx.doi.org/10.1007/b136977.

Fett, T., 2008. Stress Intensity Factors - T-Stresses - Weight Functions. In: Schriftenreihe des Instituts für Keramik im Maschinenbau - IKM, 50, Karlsruher Institut für Technologie (KIT), http://dx.doi.org/10.5445/KSP/1000007996.

Ge, T., Tzoumanekas, C., Anogiannakis, S.D., Hoy, R.S., Robbins, M.O., 2017. Entanglements in glassy polymer crazing: Cross-links or tubes? Macromolecules 50 (1), 459–471. http://dx.doi.org/10.1021/acs.macromol.6b02125.

Haward, R.N., Young, R.J., 1997. The Physics of Glassy Polymers. Springer Netherlands, Dordrecht, http://dx.doi.org/10.1007/978-94-011-5850-3.

Hempel, P., 2016. Constitutive modeling of amorphous thermoplastic polymers with special emphasis on manufacturing processes (Ph.D. thesis). KIT Scientific Publishing, Karlsruhe, http://dx.doi.org/10.5445/KSP/1000056493.

Hoare, J., Hull, D., 1972. Craze yielding and stress-strain characteristics of crazes in polystyrene. Philos. Mag. J. Theor. Exp. Appl. Phys. 26 (2), 443–455. http://dx.doi.org/10.1080/14786437208227440.

Holopainen, S., 2013. Modeling of the mechanical behavior of amorphous glassy polymers under variable loadings and comparison with state-of-the-art model predictions. Mech. Mater. 66, 35–58. http://dx.doi.org/10.1016/j.mechmat.2013.06.009.
Hund, J., 2022. Characterisation and modelling of PC/ABS blends (Ph.D. thesis). KIT Scientific Publishing, Karlsruhe, http://dx.doi.org/10.5445/KSP/1000141093.
Imai, Y., Ward, I.M., 1985. A study of craze deformation in the fatigue fracture of polymethylmethacrylate. J. Mater. Sci. 20 (11), 3842–3852. http://dx.doi.org/10.1007/BF00552372.
Ishikawa, M., Narisawa, I., 1983. Fracture of notched polycarbonate under hydrostatic pressure. J. Mater. Sci. 18 (7), 1947–1957. http://dx.doi.org/10.1007/BF00554987.
Ishikawa, M., Narisawa, I., Ogawa, H., 1977. Criterion for craze nucleation in polycarbonate. J. Polym. Sci. Polym. Phys. Ed. 15 (10), 1791–1804. http://dx.doi.org/10.1002/pol.1977.180151009.
Kambour, R.P., 1973. A review of crazing and fracture in thermoplastics. J. Polym. Sci. Macromol. Rev. 7 (1), 1–154. http://dx.doi.org/10.1002/pol.1973.230070101.
Kambour, R.P., Kopp, R.W., 1969. Cyclic stress–strain behavior of the dry polycarbonate craze. J. Polym. Sci. Part A-2 Polym. Phys. 7 (1), 183–200. http://dx.doi.org/10.1002/pol.1969.160070115.
Kausch, H.H., 1983. Crazing in Polymers. Advances in Polymer Science, Vol. 52/53, Springer, Heidelberg, http://dx.doi.org/10.1007/BFb0024054,
Kausch, H.H., 1990. Crazing in Polymers Vol. 2. Advances in Polymer Science, Springer Berlin Heidelberg, Berlin, Heidelberg, http://dx.doi.org/10.1007/BFb0018017,
Könczöl, L., Döll, W., Bevan, L., 1990. Mechanisms and micromechanics of fatigue crack propagation in glassy thermoplastics. Colloid Polym. Sci. 268 (9), 814–822. http://dx.doi.org/10.1007/BF01410959.
Kramer, E.J., Hart, E.W., 1984. Theory of slow, steady state crack growth in polymer glasses. Polymer 25 (11), 1667–1678. http://dx.doi.org/10.1016/0032-3861(84)90164-2.
Laschuetza, T., Ge, T., Seelig, T., Rottler, J., 2024. Molecular simulations of crazes in glassy polymers under cyclic loading. Macromolecules Article ASAP, http://dx.doi.org/10.1021/acs.macromol.4c01445.
Laschuetza, T., Seelig, T., 2024. A continuum-micromechanical model for crazing in glassy polymers under cyclic loading. Mech. Mater. 189, 104901. http://dx.doi.org/10.1016/j.mechmat.2023.104901.
Maiti, S., Geubelle, P.H., 2005. A cohesive model for fatigue failure of polymers. Eng. Fract. Mech. 72 (5), 691–708. http://dx.doi.org/10.1016/j.engfracmech.2004.06.005.
Mills, N.J., Walker, N., 1980. Fatigue crack initiation in glassy plastics in high strain fatigue tests. J. Mater. Sci. 15 (7), 1832–1840. http://dx.doi.org/10.1007/BF00550604.
Narisawa, I., Yee, A., 1993. Crazing and fracture of polymers. In: Materials Science and Technology, Vol. 12, pp. 699–765. http://dx.doi.org/10.1002/9783527603978.mst0146.
Pruitt, L., Suresh, S., 1993. Cyclic stress fields for fatigue cracks in amorphous solids experimental measurements and their implications. Phil. Mag. A 67 (5), 1219–1245. http://dx.doi.org/10.1080/01418619308224768.
Pulos, G.C., Knauss, W.G., 1998. Nonsteady crack and craze behavior in PMMA under cyclical loading: III. Effect of load history on cohesive force distribution on the craze. Int. J. Fract. 93 (1), 187–207. http://dx.doi.org/10.1023/A:1007569703250.
Rice, J.R., 1967. Mechanics of Crack Tip Deformation and Extension by Fatigue. Fatigue Crack Propagation, ASTM International, pp. 247–311.
Rottler, J., Robbins, M.O., 2003. Growth, microstructure, and failure of crazes in glassy polymers. Phys. Rev. E 68, 011801. http://dx.doi.org/10.1103/PhysRevE.68.011801.
Schirrer, R., Le Masson, J., Tomatis, B., Lang, R., 1984. The disentanglement time of the craze fibrils under cyclic loading. Polym. Eng. Sci. 24 (10), 820–824. http://dx.doi.org/10.1002/pen.760241012.
Sharma, R., Boyce, M.C., Socrate, S., 2008. Micromechanics of toughening in ductile/brittle polymeric microlaminates: Effect of volume fraction. Int. J. Solids Struct. 45 (7–8), 2173–2202. http://dx.doi.org/10.1016/j.ijsolstr.2007.11.023.
Skibo, M.D., Hertzberg, R.W., Manson, J.A., Kim, S.L., 1977. On the generality of discontinuous fatigue crack growth in glassy polymers. J. Mater. Sci. 12 (3), 531–542. http://dx.doi.org/10.1007/BF00540278.
Socrate, S., Boyce, M.C., Lazzeri, A., 2001. A micromechanical model for multiple crazing in high impact polystyrene. Mech. Mater. 33 (3), 155–175. http://dx.doi.org/10.1016/S0167-6636(00)00068-5.
Takemori, M.T., 1982. Fatigue fracture of polycarbonate. Polym. Eng. Sci. 22 (15), 937–945. http://dx.doi.org/10.1002/pen.760221506.
Takemori, M.T., 1990. Competition between crazing and shear flow during fatigue. In: Kausch, H.H. (Ed.), Crazing in Polymers Vol. 2. In: Advances in Polymer Science, Vol. 91/92, Springer, Heidelberg, pp. 263–300. http://dx.doi.org/10.1007/BFb0018023.
Takemori, M.T., Kambour, R.P., 1981. Discontinuous fatigue crack growth in polycarbonate. J. Mater. Sci. 16 (4), 1108–1110. http://dx.doi.org/10.1007/BF00542759.
Tijssens, M., Giessen, E.d., Sluys, L.J., 2000a. Simulation of mode I crack growth in polymers by crazing. Int. J. Solids Struct. 37 (48–50), 7307–7327. http://dx.doi.org/10.1016/S0020-7683(00)00200-6.
Tijssens, M., van der Giessen, E., Sluys, L.J., 2000b. Modeling of crazing using a cohesive surface methodology. Mech. Mater. 32 (1), 19–35. http://dx.doi.org/10.1016/S0167-6636(99)00044-7.
Ungsuwarungsri, T., Knauss, W.G., 1988. A nonlinear analysis of an equilibrium craze: Part I—Problem formulation and solution. J. Appl. Mech. 55 (1), 44–51. http://dx.doi.org/10.1115/1.3173659.
Venkatesan, S., Basu, S., 2015. Investigations into crazing in glassy amorphous polymers through molecular dynamics simulations. J. Mech. Phys. Solids 77 (46), 123–145. http://dx.doi.org/10.1016/j.jmps.2015.01.005.
Wang, W.-C.V., Kramer, E.J., 1982. A distributed dislocation stress analysis for crazes and plastic zones at crack tips. J. Mater. Sci. 17 (7), 2013–2026. http://dx.doi.org/10.1007/BF00540419.
Warren, W.E., Chudnovsky, A., Mullen, R.L., 1989. On the accuracy of the calculated stress field around a craze. Polym. Eng. Sci. 29 (6), 426–431. http://dx.doi.org/10.1002/pen.760290612.
Wu, P.D., van der Giessen, E., 1993. On improved network models for rubber elasticity and their applications to orientation hardening in glassy polymers. J. Mech. Phys. Solids 41 (3), 427–456. http://dx.doi.org/10.1016/0022-5096(93)90043-F.
Yu, W., Blair, M., 2013. DNAD, a simple tool for automatic differentiation of fortran codes using dual numbers. Comput. Phys. Comm. 184 (5), 1446–1452. http://dx.doi.org/10.1016/j.cpc.2012.12.025.